

PAPER

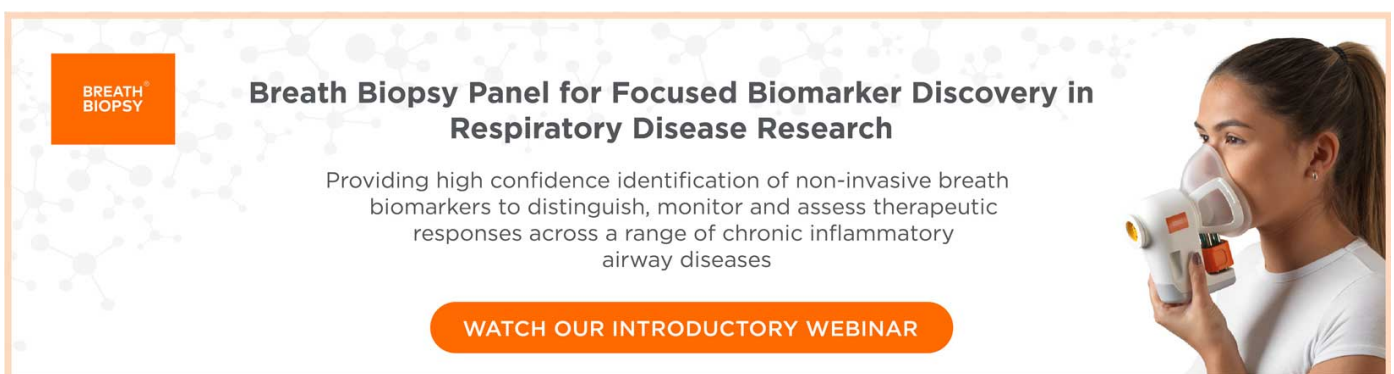
## Controlled co-delivery system of magnesium and lanthanum ions for vascularized bone regeneration

To cite this article: Ruo Chen Luo *et al* 2021 *Biomed. Mater.* **16** 065024

View the [article online](#) for updates and enhancements.

### You may also like

- [Combinatorial incorporation of fluoride and cobalt ions into calcium phosphates to stimulate osteogenesis and angiogenesis](#)  
Zeinab Tahmasebi Birgani, Nazli Gharraee, Angad Malhotra *et al.*
- [Biofabrication of vasculature in microphysiological models of bone](#)  
Ian T Whelan, E Moeendarbary, David A Hoey *et al.*
- [Delivery of dimethyloxalylglycine in calcined bone calcium scaffold to improve osteogenic differentiation and bone repair](#)  
Tujun Weng, Liangliang Zhou, Lingxian Yi *et al.*



**BREATH BIOPSY**

### Breath Biopsy Panel for Focused Biomarker Discovery in Respiratory Disease Research

Providing high confidence identification of non-invasive breath biomarkers to distinguish, monitor and assess therapeutic responses across a range of chronic inflammatory airway diseases

[WATCH OUR INTRODUCTORY WEBINAR](#)

# Biomedical Materials



## PAPER



# Controlled co-delivery system of magnesium and lanthanum ions for vascularized bone regeneration

RECEIVED  
14 July 2021

REVISED  
10 September 2021

ACCEPTED FOR PUBLICATION  
20 September 2021

PUBLISHED  
15 October 2021

Ruo Chen Luo<sup>1</sup>, Yiqian Huang<sup>2</sup>, Xiaojing Yuan<sup>1</sup>, Zuoying Yuan<sup>3</sup>, Liwen Zhang<sup>2</sup>, Janming Han<sup>4</sup>,  
Yuming Zhao<sup>1,\*</sup>  and Qing Cai<sup>2,\*</sup> 

<sup>1</sup> Department of Pediatric Dentistry, Peking University School and Hospital of Stomatology, Beijing100081, People's Republic of China

<sup>2</sup> State Key Laboratory of Organic-Inorganic Composites, Beijing Laboratory of Biomedical Materials, Beijing University of Chemical Technology, Beijing100029, People's Republic of China

<sup>3</sup> Department of Mechanics and Engineering Science, College of Engineering, Peking University, Beijing100871, People's Republic of China

<sup>4</sup> Department of Dental Materials, Peking University School and Hospital of Stomatology, Beijing100081, People's Republic of China

\* Authors to whom any correspondence should be addressed.

E-mail: [yuming\\_zhao@hotmail.com](mailto:yuming_zhao@hotmail.com) and [caiqing@mail.buct.edu.cn](mailto:caiqing@mail.buct.edu.cn)

**Keywords:** magnesium ion ( $Mg^{2+}$ ), lanthanum ion ( $La^{3+}$ ), controlled release, angiogenesis, bone regeneration

Supplementary material for this article is available [online](#)

## Abstract

For craniofacial bone regeneration, how to promote vascularized bone regeneration is still a significant problem, and the controlled release of trace elements vital to osteogenesis has attracted attention. In this study, an ion co-delivery system was developed to promote angiogenesis and osteogenesis. Magnesium ions ( $Mg^{2+}$ ) and lanthanum ions ( $La^{3+}$ ) were selected as biosignal molecules because  $Mg^{2+}$  can promote angiogenesis and both of them can enhance bone formation. Microspheres made of poly(lactide-co-glycolide) were applied to load  $La_2(CO_3)_3$ , which was embedded into a  $MgO/MgCO_3$ -loaded cryogel made of photocrosslinkable gelatin methacryloyl to enable co-delivery of  $Mg^{2+}$  and  $La^{3+}$ . Evaluations of angiogenesis and osteogenesis were conducted via both *in vitro* cell culture using human bone marrow mesenchymal stromal cells and *in vivo* implantation using a rat model with calvarial defect (5 mm in diameter). Compared to systems releasing only  $Mg^{2+}$  or  $La^{3+}$ , the combination system demonstrated more significant effects on blood vessels formation, thereby promoting the regeneration of vascularized bone tissue. At 8 weeks post-implantation, the new bone volume/total bone volume ratio reached a value of  $40.1 \pm 0.9\%$ . In summary, a properly designed scaffold system with the capacity to release ions of different bioactivities in a desired pattern can be a promising strategy to meet vascularized bone regeneration requirements.

## 1. Introduction

Oral and maxillofacial tumors, bone infections and trauma can cause bone defects and interruption of the local blood supply, and a functional network of blood vessels is necessary for provision of oxygen and nutrients to promote osteogenesis [1]. Thus, therapeutic targeting of the angiogenic response is essential to enhance bone regeneration [2]. A lack of neovascularization lead to delayed healing and even cause the ultimate failure of osteogenesis [3].

In bone tissue engineering, delivery systems of growth factors are often applied to promote the regeneration of vascularized bone tissue [4, 5].

Studies have shown that compared to simultaneous release, the co-delivery of vascular factors and bone growth factors has a better effect on bone formation [4, 6, 7]. When vascular endothelial growth factor (VEGF) is released at a faster rate in the early stage, it can promote angiogenesis; while the sustained release of BMP-2 in the later stage can promote vascularized bone regeneration [8, 9]. However, the short half-life and high synthesis costs of growth factors limit their application [10]. Loading trace elements is an efficient approach for promoting bone regeneration [11]. Some trace elements play functional roles in the physiological cellular environment and have the potential to promote angiogenesis and osteogenesis

[12, 13]. What's more, they are stable during scaffold preparation and have high efficiency even at low concentrations [14].

Magnesium is the second most abundant metal element in natural bone besides calcium, and it is an important component taking part in bone development and maturation [15]. Magnesium ions ( $Mg^{2+}$ ) are directly involved in many biological mechanisms; for example, they play important roles in regulation of ion channels and stimulation of cell growth and proliferation [16]. Numerous studies have shown that approximately 10 mM  $Mg^{2+}$  can promote angiogenesis [17–19].  $Mg^{2+}$  can promote the proliferation and migration of capillary endothelial cells [20, 21] and make them sensitive to migration signals, thereby inducing key events in angiogenesis [22]. Additionally,  $Mg^{2+}$  can promote mesenchymal stromal cell (MSC) proliferation and induce osteogenic differentiation [23, 24]. To fabricate  $Mg^{2+}$ -releasing scaffolds for bone tissue engineering, Mg metal [25] or Mg-containing compounds have been loaded into biodegradable polymers [26]. Because the degradation rate of Mg metal is fast and produces hydrogen gas that is not so welcomed for *in vivo* application [27], the mixture of Mg-containing compounds such as MgO and  $MgCO_3$  is likely selected by researchers to achieve controlled release of  $Mg^{2+}$  due to their different solubility [24].

Apart from  $Mg^{2+}$ , in recent years, lanthanides have also been discovered to have significant effects on bone formation [28, 29]. Lanthanides are functional simulators of calcium ions ( $Ca^{2+}$ ) that have similar ionic radii and almost the same coordination numbers of protein binding sites [30].  $La^{3+}$  can promote osteogenic differentiation at concentrations as low as  $10^{-9}$ – $10^{-7}$  M [29, 31], and this concentration is much lower than that of  $Ca^{2+}$  as it being effective in regulating cell behaviors [32]. Lanthanides have strong interactions with inorganic phosphates such as hydroxyapatite [33], and they are considered as guiding elements of bone tissue that can regulate the differentiation of osteoblasts and osteoclasts [34]. For example, the release of  $La^{3+}$  from chitosan-based scaffolds has been found to promote bone regeneration in a rat skull defect model [35]. The mechanical properties of the scaffold were even improved with the incorporation of La-containing compounds such as  $La_2(CO_3)_3$ , which might be an extra merit for bone repair [36].

Due to the diverse functions of different elements, a co-delivery system designed for the controlled release of different trace elements is an attractive option for achievement of satisfactory regeneration of vascularized bone tissue [37, 38]. Co-delivery of bioactive factors is preferred for promotion of angiogenesis and subsequent enhancement of osteogenesis [39]. Scaffolds fabricated with designs such as core-shell structures or using the composite strategy (e.g. hydrogel-microsphere systems) were readily able to

obtain co-delivery by embedding the compounds in different parts of the scaffolds [40–42]. As well known, the hydrophilic matrix would bring a faster release rate for hydrophilic compounds, while a hydrophobic matrix would retard the release. Herein, it was proposed to incorporate MgO/ $MgCO_3$  into a porous cryogel-type scaffold with  $La_2(CO_3)_3$ -loaded microspheres being introduced simultaneously, from which, the fast release of  $Mg^{2+}$  and subsequent release of  $La^{3+}$  were expected. Following our previous report [24], the weight fraction of MgO/ $MgCO_3$  was set as 1:1 to obtain a desirable  $Mg^{2+}$  release behavior.

Photocrosslinkable gelatin-methacryloyl (GelMA) was used to produce the cryogel because of the popularity of GelMA in various biomedical applications [43–45]. Cryogels are highly porous scaffolds with interconnected pores, favoring cell infiltration, attachment, and proliferation [40]. Cells could easily interact with  $Mg^{2+}$  released from cryogels to accelerate angiogenesis [46]. FDA-approved biodegradable poly(lactide-co-glycolide) (PLGA) was applied to prepare  $La_2(CO_3)_3$ -loaded microspheres [47], and the gradually released  $La^{3+}$  would contribute to osteogenesis at a later stage, meeting the rhythm of vascularized bone regeneration [48, 49]. With these designs, comprehensive characterizations were conducted on the composite scaffolds in terms of  $Mg^{2+}/La^{3+}$  release test, cell viability and angiogenic/osteogenic differentiation responses of human bone marrow MSCs (hBMSCs) in relation to the  $Mg^{2+}/La^{3+}$  concentrations, *in vitro/in vivo* blood vessel formation via Matrigel culture and subcutaneous implantation in mice, and finally neo-bone formation in rat calvarial defect model. The positive hypothesis of this study was that, a scaffold with the capacity to co-delivery  $Mg^{2+}/La^{3+}$  in an optimized manner would be able to significantly enhance the regeneration of vascularized bone tissue.

## 2. Materials and methods

### 2.1. Material preparation

MgO,  $MgCO_3$ ,  $La_2(CO_3)_3$  and gelatin (type A, from porcine skin, ~300 g Bloom) were purchased from Sigma-Aldrich (USA). Methacrylic anhydride and 2-hydroxy-4'-(2-hydroxyethoxy)-2-methylpropiophenone (I2959) were purchased from Aladdin (China). PLGA (lactide:glycolide = 75:25, MW = 50 000) was purchased from Shandong Pharmaceutical Sciences Pilot Plant (China). All other reagents and solvents used were of analytical grade and supplied by Beijing Chemical Reagent Co. Ltd (China).

#### 2.1.1. Preparation of $La_2(CO_3)_3$ -loaded PLGA microspheres

$La_2(CO_3)_3$ -loaded PLGA microspheres were prepared by the (S/O)/W emulsion technique<sup>24</sup> [50].

PLGA (1 g) was dissolved in 20 ml of dichloromethane ( $\text{CH}_2\text{Cl}_2$ ). After 8 h of magnetic stirring, Span 80 (20 mg) and  $\text{La}_2(\text{CO}_3)_3$  (100 mg) were added to the solution. Then, the suspension was added to 200 ml of 1% wt/vol poly(vinyl alcohol) (PVA) solution containing Tween 60 (20 mg) under stirring (300 rpm). After 4 h of solvent evaporation at room temperature, the microspheres were collected, washed, and then lyophilized for further use.

### 2.1.2. Synthesis of GelMA

GelMA was synthesized as reported [45]. Gelatin (20 g) was dissolved in 200 ml of PBS thermostatically maintained at 50 °C, into which, 20 ml of methacrylic anhydride was dripped under constant stirring. The reaction was continued for 4 h at 50 °C to obtain GelMA, which was purified by dialysis and then lyophilized for later use.

### 2.1.3. Preparation of $\text{Mg}^{2+}/\text{La}^{3+}$ co-delivery cryogel-type scaffold

GelMA (1 g) was dissolved in 10 ml of deionized water with 0.2 wt/vol% I2959 (photoinitiator) added. The mixed powder of  $\text{MgO}/\text{MgCO}_3$  (1:1 in weight) was blended with the GelMA solution at different mass fractions (0 wt%, 2 wt%, 5 wt%) in relation to the dry weight of the GelMA. The suspensions (200 ml) were transferred into the wells of 24-well plates, frozen at -20 °C for 24 h, and exposed to 365 nm ultraviolet light for 10 min (40 mW  $\text{cm}^{-2}$ ) to initiate photocrosslinking. Then, the systems were submitted to lyophilization to obtain Mg-containing GelMA cryogels, which were termed as M0, M2 and M5 for simplification. Based on the M0 cryogel, La-containing GelMA cryogels were prepared similarly, with  $\text{La}_2(\text{CO}_3)_3$ -loaded PLGA microspheres being added at 10 wt% and 20 wt% fractions into the GelMA solution before cryogel formation; the resulting cryogels were accordingly termed as P10 and P20 for simplification. For the preparation of  $\text{Mg}^{2+}/\text{La}^{3+}$  co-delivery GelMA cryogels (figure 1), 10 wt%  $\text{La}_2(\text{CO}_3)_3$ -loaded PLGA microspheres were introduced into M2 and M5 cryogels to obtain M2P10 and M5P10 scaffolds.

## 2.2. Characterizations

After the samples were fabricated and freeze-dried, the morphology of microspheres and cryogels was observed under a scanning electron microscope (SEM, SU8010, HITACHI, Japan). The mean diameters of microspheres and the mean pore sizes of cryogels were estimated by measuring 300 microspheres or pores from SEM images using ImageJ software. Elemental mapping was performed with the same parameters as SEM observation.

## 2.3. Degradation studies

For degradation studies, cryogels ( $D = 10$  mm,  $H = 1$  mm) were weighed ( $W_0$ ) and then immersed in 2 ml of PBS ( $n = 4$ ). The systems were placed in

a 37 °C water bath for 12 weeks with refreshment of the PBS every week. Samples were collected at 6 and 12 weeks, washed with deionized water, freeze-dried and weighed ( $W_d$ ) before SEM observation. Elemental mapping was performed with the same parameters as SEM observation. Weight loss (%) was calculated as  $(W_0 - W_d)/W_0 \times 100$ .

## 2.4. $\text{Mg}^{2+}$ and $\text{La}^{3+}$ release test

To evaluate the release behaviors of  $\text{Mg}^{2+}$  and  $\text{La}^{3+}$ , cryogels ( $D = 10$  mm,  $H = 1$  mm) were immersed in PBS (2 ml for each piece) and kept at 37 °C for 28 d, each cryogel group had 4 replicate samples ( $n = 4$ ). On day 3, 7, 14, 21 and 28, 1 ml of sample medium was collected for each sample; at the same time, 1 ml of fresh PBS was added to the system, and the release test was continued. The pH value of the retrieved medium was measured with a pH meter (Hanna, Italy). The retrieved medium was then diluted to 20 ml with fresh PBS and analyzed by inductively coupled plasma optical emission spectrometry (Perkinelmer, Optima 7000DV, USA).

## 2.5. Extract preparation for cell culture

According to the International Organization for Standardization (ISO10993-12), extracts from different cryogels were prepared for subsequent cell culture studies. The cryogels were sterilized by soaking in 75% ethanol with ultraviolet irradiation for 4 h and washed in PBS overnight. Each piece of cryogel ( $D = 10$  mm,  $H = 1$  mm) was immersed in 2 ml of  $\alpha$ -modified Eagle medium ( $\alpha$ -MEM, Gibco, USA) to culture hBMSCs or Medium 199 (M199, Gibco, USA) to culture human umbilical vein endothelial cells (HUVECs) at 37 °C for 24 h, and then extract was collected to prepare the cell culture medium (extract containing 10% FBS) or osteoinduction medium (extract containing 15% FBS (Gibco, USA), 50 mg  $\text{ml}^{-1}$  L-ascorbic acid, 10 mM  $\beta$ -glycerol and 100 mmol  $\text{L}^{-1}$  dexamethasone (Sigma, USA)).

## 2.6. Cell proliferation

The HUVECs and hBMSCs used in this study were purchased from CHI Scientific, Inc. (China). To evaluate the influence of released  $\text{Mg}^{2+}$ ,  $\text{La}^{3+}$  and  $\text{Mg}^{2+}/\text{La}^{3+}$  together on cell proliferation,  $5 \times 10^3$  hBMSCs were seeded into each well in 96-well plates and cultivated in  $\alpha$ -MEM medium (100  $\mu\text{l}$ ) containing 10% FBS for 24 h to enable cell attachment ( $n = 5$ ). After that, the medium in each cell was replaced with extracts prepared from different cryogels using  $\alpha$ -MEM to continue the cell culture, during which the extract was refreshed every two days. To measure the proliferation of cells after 1, 4 and 7 d, Alamar blue (Solarbio, China) was used to incubate the cells at 37 °C in the dark for 2 h, and then the fluorescence value of the solution was measured with a microplate reader.

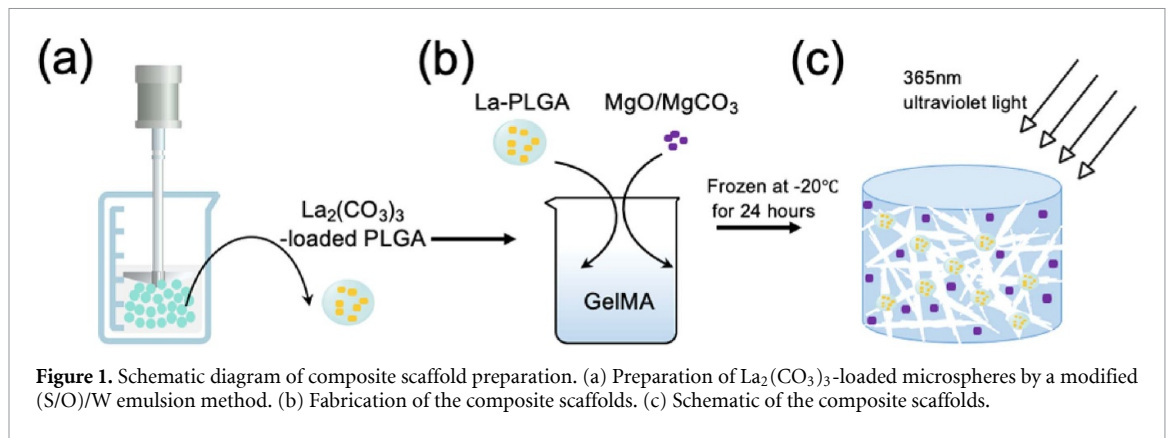


**Figure 1.** Schematic diagram of composite scaffold preparation. (a) Preparation of  $\text{La}_2(\text{CO}_3)_3$ -loaded microspheres by a modified (S/O)/W emulsion method. (b) Fabrication of the composite scaffolds. (c) Schematic of the composite scaffolds.

### 2.7. Cell viability

To evaluate the compatibility of the scaffolds, the viability of cells was observed by live/dead staining and phalloidin-Hoechst/DAPI staining. Each cryogel group ( $D = 10$  mm,  $H = 1$  mm) was placed into a 48-well plate, sterilized by soaking in 75% ethanol with ultraviolet irradiation for 4 h, washed in PBS and immersed in  $\alpha$ -MEM overnight. Subsequently,  $1 \times 10^4$  hBMSCs were seeded onto the surface of the scaffold in each well. After 1, 4, and 7 d, a calcein-AM/PI double staining kit (Solarbio, China) was used to evaluate cell viability, and fluorescence images were obtained with a confocal laser scanning microscope (CLSM, TCS-SP8 STED 3X, Leica, Germany). For cell morphology evaluation, actin was stained with 100 nm TRITC-phalloidin (Yeasen, China), and nuclei were counterstained with  $10 \mu\text{g ml}^{-1}$  DAPI (Solarbio, China). Fluorescence images were captured with the CLSM. Five visual fields ( $0.7 \times 0.7$  mm) were randomly selected for observation under microscope, and the five visual fields were statistically analyzed by ImageJ software ( $n = 5$ ).

### 2.8. Cell migration

Transwell migration assays were used to verify the effects of released ions on cell migration ability. Each group of samples ( $D = 10$  mm,  $H = 1$  mm) was placed into the lower chamber (Corning, USA), and  $2 \times 10^4$  HUVECs were added to each upper chamber. Next, 500  $\mu\text{l}$  of M199 was added to each well. After 10 h of incubation at  $37^\circ\text{C}$ , the upper chamber was taken out and put into 4% paraformaldehyde fix solution for 20 min. The cells on the upper surface were wiped with a cotton swab, and crystal violet staining was conducted to observe the cells that migrated through the membrane's pores. Five visual fields ( $0.9 \times 0.6$  mm) were randomly selected for observation under microscope, and the five visual fields were statistically analyzed by ImageJ software ( $n = 5$ ).

### 2.9. *In vitro* osteogenesis assay

For the *in vitro* osteogenic differentiation experiment, cryogels ( $D = 10$  mm,  $H = 1$  mm) were

placed in 24-well plates and sterilized, and  $5 \times 10^4$  hBMSCs were seeded onto the surface of each scaffold, the cells were directly seeded on the tissue culture polystyrene (TCPs) as control. Osteoinduction medium ( $\alpha$ -MEM containing 50  $\text{mg ml}^{-1}$  L-ascorbic acid, 10 mM  $\beta$ -glycerol and 100  $\text{mmol L}^{-1}$  dexamethasone) was added to each well and refreshed every two days. Alkaline phosphatase (ALP) staining (Beyotime, China) was performed on the 7th day of culture to observe ALP activity. The cells were fixed with 4% paraformaldehyde fixative for 30 min, and then incubated with Alkaline Phosphatase Assay Kit (Beyotime, China) for 10 min in the dark, and then photographed for observation. The formation of calcium nodules was observed by alizarin red staining (ARS) on the 14th day of culture. The cells in each well were immersed in Alizarin red working solution (1% wt/vol) for 10 min. The cryogels of each group without cell seeding were stained under the same conditions to eliminate the influence of dye adsorption by the cryogels. After staining with alizarin red solution, the samples were washed with PBS and incubated with 10% cetylpyridinium chloride solution (Sigma, USA) for 30 min to determine solution absorbance for the quantitative analysis of ARS.

For the quantitative polymerase chain reaction (qPCR) assay, on the 7th and 14th days of osteoinduction culture, total RNA was extracted by adding 300  $\mu\text{l}$  of Trizol to each well, and then reverse transcription was performed for PCR analysis ( $n = 4$ ). Four genes, *GAPDH*, *ALP*, osteocalcin (*OCN*) and collagen I (*COL-1*), were evaluated by real-time qPCR (ABI7500, Thermo Fisher Scientific, USA), the Ct values of different groups was analyzed by the  $2^{-\Delta\Delta\text{Ct}}$  method, and their specific primers were designed as listed in table. S1.

### 2.10. *In vitro* angiogenesis assay

*In vitro* tube formation was examined using a Matrigel (Corning) assay. Matrigel was added to a 24-well plate at a volume of 300  $\mu\text{l}$  per well and incubated at  $37^\circ\text{C}$  for 30 min. HUVECs ( $5 \times 10^4$ ) were cultured in each well with extracts made from different cryogels using M199 for 9 h to observe vessel formation

under an optical microscope (TE2000-U, Olympus, Japan), the cells were cultured in the  $\alpha$ -MEM as control. The images were analyzed with AngioTool software to measure the lengths of the formed tubes.

For the qPCR assay, cryogels ( $D = 10$  mm,  $H = 1$  mm) were placed in 24-well plates and sterilized, and HUVECs ( $5 \times 10^4$  per well) were seeded on the surface of each cryogel and cultured for 7 and 14 d, the cells are directly seeded on TCPs as control. At predetermined intervals, the cell samples were lysed with Trizol to extract RNA for analysis of the expression of VEGF in relation to GAPDH using qPCR ( $n = 4$ ).

### 2.11. *In vivo* angiogenesis assay

All animal experiments (rats, mice) were approved by the Ethics Committee of Peking University School of Medicine (China, approval number: LA2019325). Cryogels ( $D = 6$  mm,  $H = 1$  mm) were transplanted subcutaneously into the backs of 6 week-old male Balb/C nude mice. The experimental groups were the M0, M2P10 and M5P10 groups, with three mice in each group. At 4 weeks post implantation, the nude mice were decapitated, and the subcutaneous samples were fixed in 10 wt% neutral formalin for 24 h. The samples were then dehydrated, embedded in paraffin, sectioned for hematoxylin–eosin (HE) and Masson's trichrome staining (Solarbio, China), and observed under an inverted microscope (Olympus IX-70, NY, USA). Immunohistochemical analysis was conducted for CD31 to assess angiogenesis *in vivo*. CD31 was detected by applying anti-CD31 (Abcam, UK, cat. no. ab182981) primary antibodies at 1:500 dilutions with Antibody Diluent (ZSGB-BIO, China).

Fertilized eggs were used for chick embryo chorioallantoic membrane (CAM) assay. On the 7th day of incubation in an environment of 37.5 °C and 60% relative humidity, the eggs were placed on the ultraclean workbench, a circular incision with a diameter of 2 cm above the air chamber was made with a scalpel, then the surface film was removed with ophthalmic forceps, and 200  $\mu$ l of each group of extracts were added into different eggs. The blank control group was added with 200  $\mu$ l PBS, and the positive group was added with 200  $\mu$ l HUVECs suspension. After 5 d incubation, we removed the paraffin, prepared the fixative by mix isoacetone and acetone in a ratio of 1:1 and added the fixative to the CAM for 15 min, and placed them on a glass slide for microscope observation. The number of blood vessels were analyzed by ImageJ.

### 2.12. Critical-sized calvarial defect model

A model of calvarial defect (5 mm in diameter) was established in 7 week-old male standard deviation (SD) rats. In short, the rats were shaved and anesthetized with 1% pentobarbital sodium. The 5 mm critical defect was prepared with a trephine bur on both sides of the midline of the calvarium. The three groups

were the blank control, M0 and M2P10 groups. After each group of samples was packed into the defect site, the skin was sutured with a 5–0 absorbable surgical suture. Six rats were randomly selected from each group for analysis at 4 and 8 w ( $n = 6$ ); a total of 36 rats were observed at the two time points. The rats were sacrificed at each time point by carbon dioxide inhalation, and the calvarium of each rat was collected and fixed in 10 wt% neutral formalin buffer for 48 h for further evaluations.

The calvarium was scanned and analyzed by micro-CT (Inveon, Siemens, Germany) and the three-dimensional (3D) visualization software Inveon Research Workplace to detect the formation of new bone. The bone volume fraction (BV/TV) and bone mineral density (BMD) of the selected region of interest were quantitatively analyzed after 3D reconstruction. After micro-CT scanning analysis, decalcification treatment was carried out with 17% EDTA at 37 °C. The solution was changed every two days. After one month, the skulls were dehydrated and embedded in paraffin. Histological and immunohistochemical analyses were performed after sectioning. Histological analysis included HE staining and Masson trichrome staining. Immunohistochemical analysis was conducted for CD31 to assess angiogenesis and OCN to assess osteogenesis *in vivo*. CD31 and OCN were detected by applying anti-CD31 (Abcam, UK, cat. no. ab182981) and anti-OCN (Proteintech, UK, cat. no. 23 418-1-AP) primary antibodies at 1:500 dilutions with Antibody Diluent (ZSGB-BIO, China). Sections were then treated with an anti-rabbit secondary antibody (ZSGB-BIO, China, PV9001) and visualized with 3,3-diaminobenzidine (DAB kit, ZSGB-BIO, China).

### 2.13. Statistical analysis

The results are presented as the mean  $\pm$  SD. Statistical analysis was performed using one-way ANOVA with Tukey's post hoc test to assess differences between groups.  $P < 0.05$  was considered to indicate significance. For data at a single time point, One-way ANOVA was used to analyze single factor variance; for data at multiple time points, Two-way ANOVA was used for double factors variance analysis.

## 3. Results

### 3.1. Microstructure of Mg<sup>2+</sup>/La<sup>3+</sup>-loaded composite cryogels

The preparation of the Mg<sup>2+</sup>/La<sup>3+</sup> co-loaded composite cryogels included two steps, i.e. the preparation of La<sub>2</sub>(CO<sub>3</sub>)<sub>3</sub>-loaded PLGA microspheres and the formation of the GelMA cryogel. The microspheres were prepared using an (S/O)/W emulsion method, in which, La<sub>2</sub>(CO<sub>3</sub>)<sub>3</sub> powder was homogeneously dispersed in PLGA/CH<sub>2</sub>Cl<sub>2</sub> solution, followed by dispersing the suspension into water phase to obtain the products after solvent

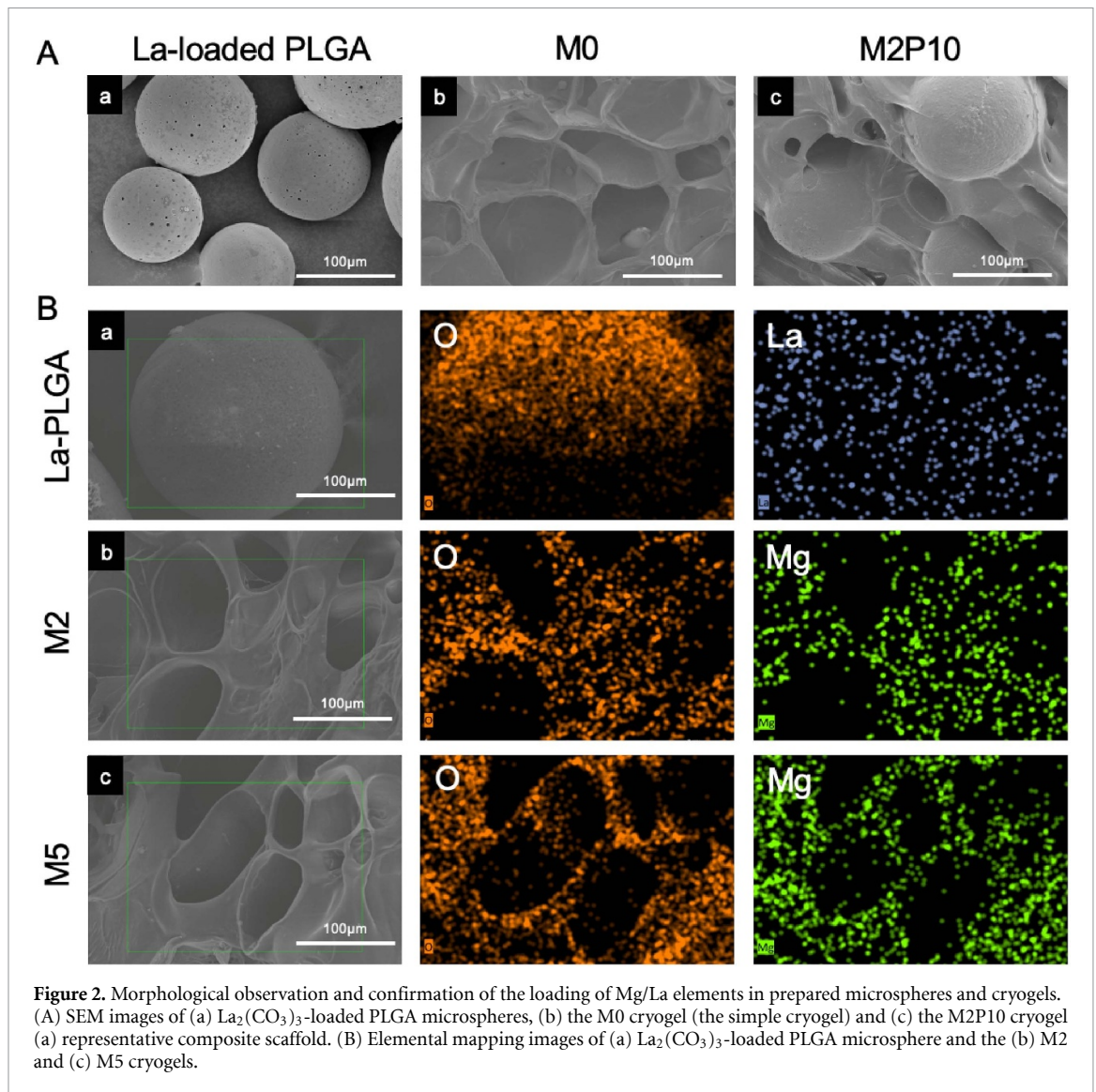
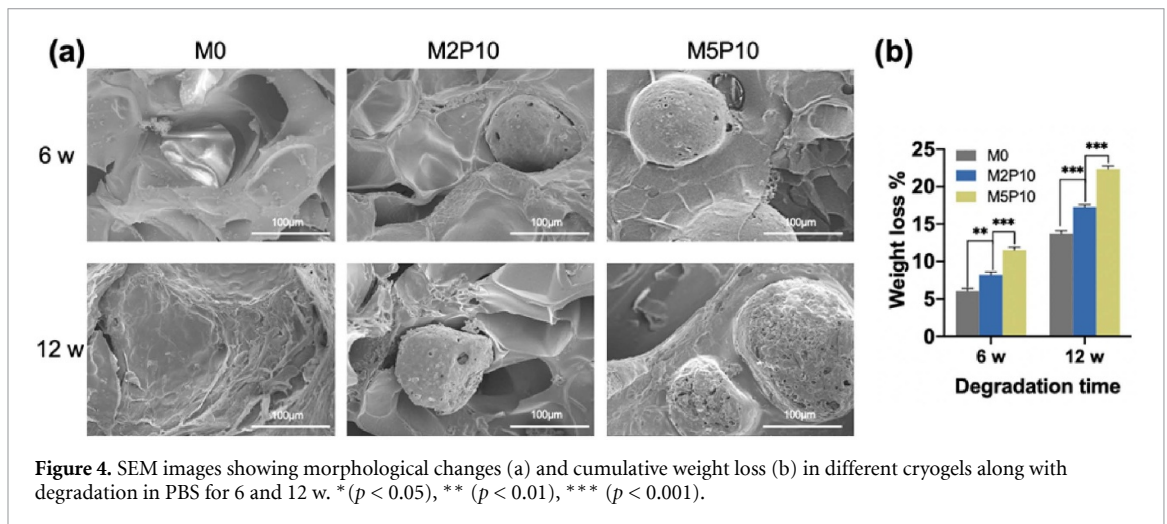
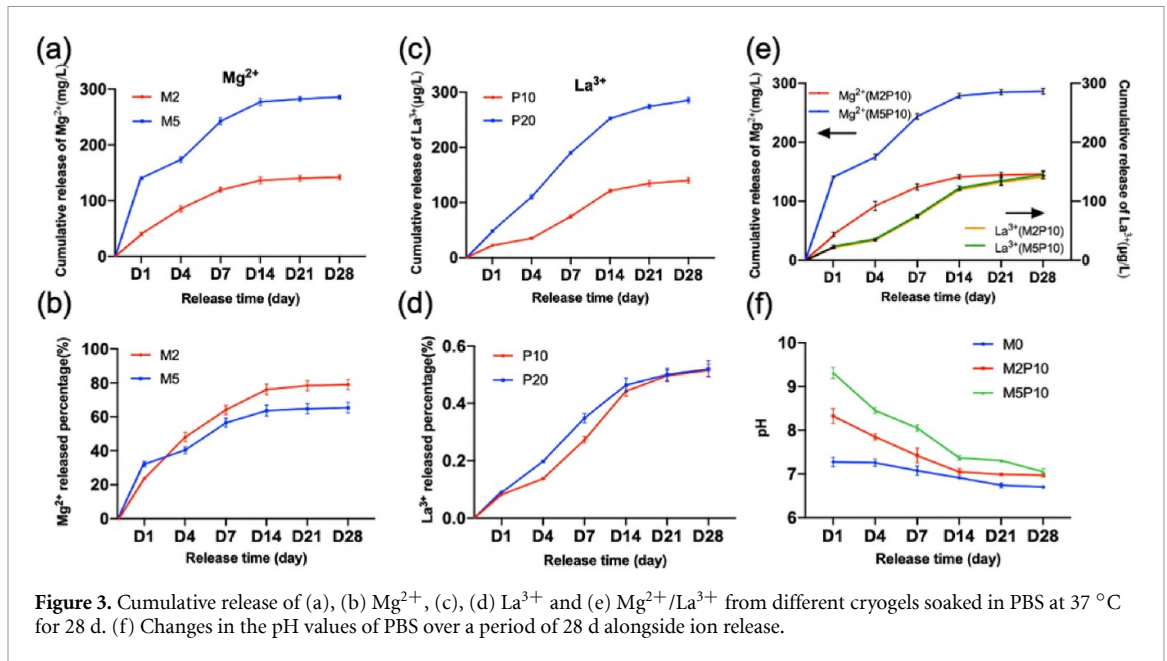


**Figure 2.** Morphological observation and confirmation of the loading of Mg/La elements in prepared microspheres and cryogels. (A) SEM images of (a)  $\text{La}_2(\text{CO}_3)_3$ -loaded PLGA microspheres, (b) the M0 cryogel (the simple cryogel) and (c) the M2P10 cryogel (a) representative composite scaffold. (B) Elemental mapping images of (a)  $\text{La}_2(\text{CO}_3)_3$ -loaded PLGA microsphere and the (b) M2 and (c) M5 cryogels.

evaporation. As shown in figure 2(A)(a), the microspheres displayed a slightly rough surface with a diameter of  $92.3 \pm 24.87 \mu\text{m}$ . The element mapping image showed that La was evenly distributed within the microsphere without apparent aggregation (figure 2(B)(a)). Cryogel with interconnected pores was prepared via freezing of the GelMA solution and subsequent photocrosslinking under frozen conditions followed by removal of ice crystals via lyophilization. As shown in figure 2(A)(b), the M0 cryogel displayed a porous structure with a pore diameter of  $95 \pm 31.7 \mu\text{m}$ . The M2 and M5 cryogels were prepared by introducing MgO/MgCO<sub>3</sub> into the GelMA solution before the freezing step, and strong signals in the elemental mapping images revealed the presence of Mg throughout the cryogels in different amounts. Finally, the  $\text{La}_2(\text{CO}_3)_3$ -loaded PLGA microspheres were dispersed into the GelMA cryogels, as shown in figure 2(A)(c), the microspheres were embedded well within the cryogel, but their locations did not destroy the overall pore structure of the cryogel.

### 3.2. Release behaviors of $\text{Mg}^{2+}$ and $\text{La}^{3+}$

The results for  $\text{Mg}^{2+}$  release from the M2 and M5 cryogels are shown in figures 3(a) and (b). The M2 cryogel released approximately  $30\text{--}50 \text{ mg L}^{-1} \text{ Mg}^{2+}$  at the initial stage, while the M5 cryogel released  $50\text{--}150 \text{ mg L}^{-1} \text{ Mg}^{2+}$  within the first 1–7 d. The difference in  $\text{Mg}^{2+}$  release between the two cryogels was consistent with the MgO/MgCO<sub>3</sub> loading of the respective cryogels, and an initial burst release was observed due to the hydrophilic feature of GelMA. The results for  $\text{La}^{3+}$  release from the P10 and P20 cryogels are shown in figures 3(c) and (d). The  $\text{La}^{3+}$  release rate was slower than the  $\text{Mg}^{2+}$  release rate. On the first day, only  $5\text{--}10$  and  $20 \mu\text{g L}^{-1} \text{ La}^{3+}$  ions were released from the P10 and P20 cryogels, respectively. The release rates of  $\text{La}^{3+}$  gradually increased with increasing soaking time, and the cumulatively released  $\text{La}^{3+}$  reached values of over  $100$  or  $200 \mu\text{g L}^{-1}$  for the P10 and P20 cryogels. In comparison, the release of  $\text{La}^{3+}$  lagged behind that of  $\text{Mg}^{2+}$ . This phenomenon was likely due to the hydrophobicity of PLGA and the shielding



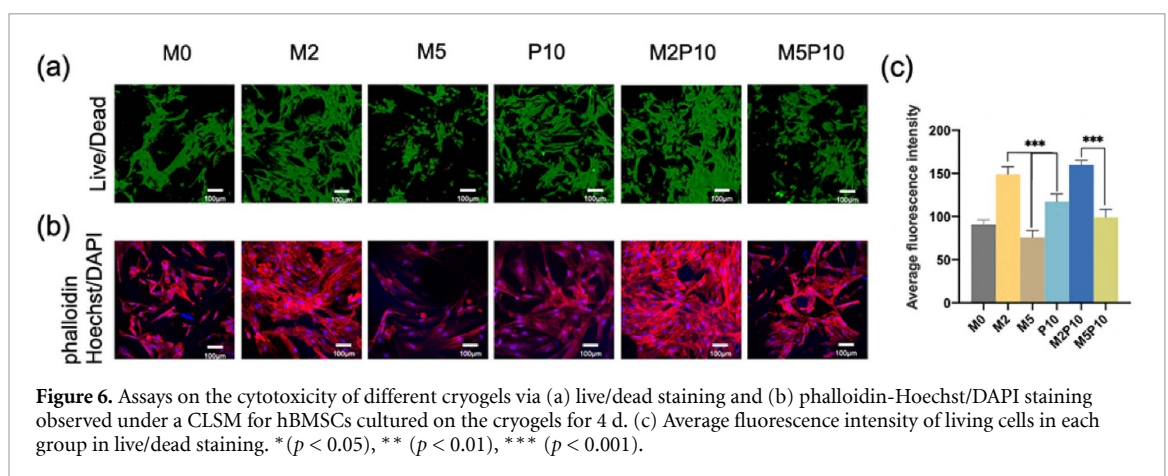
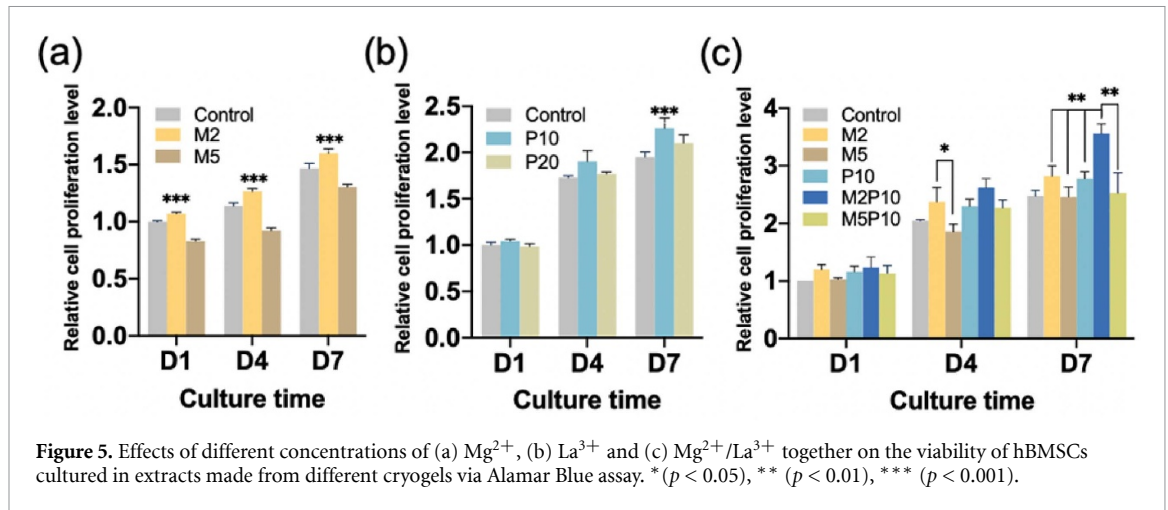
effect of the GelMA cryogel on the microspheres. From figure 3(e), it was identified that the release of  $Mg^{2+}/La^{3+}$  from M2P10 and M5P10 cryogels were comparable to corresponding M2/M5 and P10 cryogels. With the release of  $Mg^{2+}/La^{3+}$ , as shown in figure 3(f), the pH value of the soaking medium initially increased rapidly and then declined gradually as the medium was diluted with fresh PBS at every sample collection timepoint. The pH value was higher in the M5P10 group than in the M2P10 group, which was ascribed to the higher amounts of  $Mg^{2+}/La^{3+}$  in the former case because  $MgO/MgCO_3$  and  $La_2(CO_3)_3$  are alkaline substances. The cumulative release percentage of  $Mg^{2+}$  in the M2 group reached 79.4%, and that in the M5 group reached 66.9%. The cumulative release percentages of  $La^{3+}$  in the P10 and P20 groups were nearly 0.5%.

### 3.3. Degradation behaviors

A degradation study was conducted on the M0, M2P10 and M5P10 cryogels in PBS. As shown in

figure 4(a), the porous structure of the M0 cryogel remained similar to the original morphology after 6 w of soaking, while it began to become rougher and collapsed at 12 w. The morphological change in the cryogel matrix in the M2P10 sample was comparable with that in the M0 cryogel. Alongside degradation, the appearance of the PLGA microspheres also changed that the formation of pores on the microsphere surface was evident at 6 w, and a deformed spherical shape was observed at 12 w. The results of quantitative analysis of the sample weight loss are plotted in figure 4(b). The weight loss increased for all the samples as the immersion time in PBS increasing. The highest weight loss was found for the M5P10 cryogel, followed by the M2P10 and M0 cryogels. As shown in figure 3, the results suggested that the release of  $Mg^{2+}/La^{3+}$  (mainly  $Mg^{2+}$ ) contributed to sample weight loss in addition to GelMA and PLGA degradation. The increased loading of the inorganic components led to the accelerated weight loss of the corresponding cryogels





due to the gradual dissolution of  $MgO/MgCO_3$  and  $La_2(CO_3)_3$ .

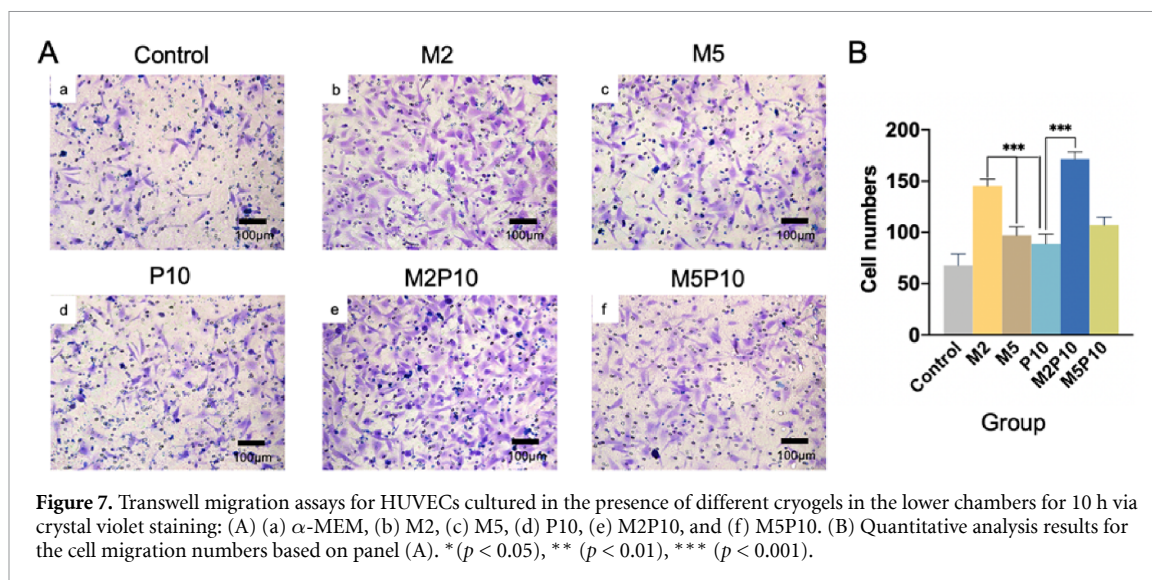
As shown in figure S1 (available online at [stacks.iop.org/BMM/16/065024/mmedia](https://stacks.iop.org/BMM/16/065024/mmedia)), the elemental fluorescence intensity of both  $Mg^{2+}$  and  $La^{3+}$  gradually decreased as the degradation proceeding. The fluorescence intensity of  $Mg^{2+}$  decreased significantly at 6 w compared to the sample of 0 w, indicating that most of the  $Mg^{2+}$  had been released at 6 w. Alongside the degradation of PLGA microspheres, sustained release of  $La^{3+}$  was also detected as its fluorescence intensity gradually decreasing from 0 to 12 w.

### 3.4. Cell viability and migration

To evaluate the potential cytotoxicity of different cryogels, extracts were made to culture hBMSCs, and cell proliferation was determined. The extracts were obtained by soaking cryogels in culture medium for 24 h. As shown in figure 3, it was estimated that the  $Mg^{2+}$  concentrations were approx.  $30\text{--}50\text{ mg L}^{-1}$  for the M2 and M2P10 extracts and approx.  $50\text{--}150\text{ mg L}^{-1}$  for the M5 and M5P10 extracts, while the  $La^{3+}$  concentrations were approx.  $50\text{--}100\text{ }\mu\text{g L}^{-1}$  and  $100\text{--}200\text{ }\mu\text{g L}^{-1}$  for the P10 and P20 extracts, respectively. Compared to the control, figure 5(a)

shows that the M2 extract significantly promoted cell proliferation, while the M5 extract exerted some adverse effects on cell growth. Both the P10 and P20 extracts enhanced cell proliferation, but the P10 extract showed a better result (figure 5(b)). Reasonably, as shown in figure 5(c), the M2P10 extract accelerated the growth of hBMSCs the most markedly among all the groups, moreover, it exerted a synergistic effect. For the M5 and M5P10 samples, the results suggested that the elevated ion concentrations and pH values of the extracts ( $pH > 9$ ) inhibited cell proliferation.

To verify material biocompatibility, hBMSCs were seeded on the surface of the material. On the 4th day, live/dead staining and phalloidin-Hoechst/DAPI staining were performed to observe cell viability with a CLSM. As shown in figure 6(a), green fluorescence was visible on the surface of the scaffold, indicating that hBMSCs survived on the surface in each group, and some red fluorescence was seen in the M5 and M5P10 groups, which indicated the presence of dead cells. The green fluorescence was the most widely distributed in the M2P10 group, which was consistent with cell proliferation results. Live/dead staining for hBMSCs cultured on the cryogels for 1, 4, 7 d showed that cells in M2P10 group proliferate faster than those



in M5P10 group (figure S2). As shown in figure 6(c), the fluorescence intensity of living cells in M2 and M2P10 groups was the highest. There is less red fluorescence in the visual field, which indicated that the material does not cause apoptosis, but it would affect the proliferation rate. As shown in figure 6(b), phalloidin-Hoechst/DAPI staining showed that each group had blue fluorescence, indicating nuclei, with different fluorescence intensities. Red fluorescence was superimposed on blue fluorescence to indicate the cytoskeleton. The greatest blue and red fluorescence distribution was observed in the M2 group and M2P10 group. As shown in figure 6(c), the green fluorescence intensity of M2 and M2P10 groups was significantly higher than that of other groups.

HUVECs were used in Transwell migration assays to verify the effects of the scaffold materials on cell migration. The results of crystal violet staining showed that the M2P10 group had the highest number of migrated cells, followed by the M2 group (figure 7). The number of migrating cells in the M2 group was significantly higher than those in the M5 and P10 groups, suggesting that the M2 group promoted cell migration.

### 3.5. *In vitro* osteogenesis

The expression of three osteogenic genes, *ALP*, *COL-1* and *OCN*, was detected by qPCR on the 7th and 14th days of osteoinduction. As shown in figures 8(a)–(c), the expressions of the *ALP*, *COL-1* and *OCN* genes were higher on the 14th day than on the 7th day. After 7 and 14 d of culture, the hBMSCs in the M2 group achieved higher expressions of the three osteogenic genes than the cells in the M5 group. The gene expression of the P10 group was higher than that of the M0 group, and the difference was more obvious after 14 d of culture than after 7 d of culture. The gene expression of the M2P10 group was significantly higher than those of the M2 and P10 groups. As shown in 8(e), Images of ALP staining at 7 d showed

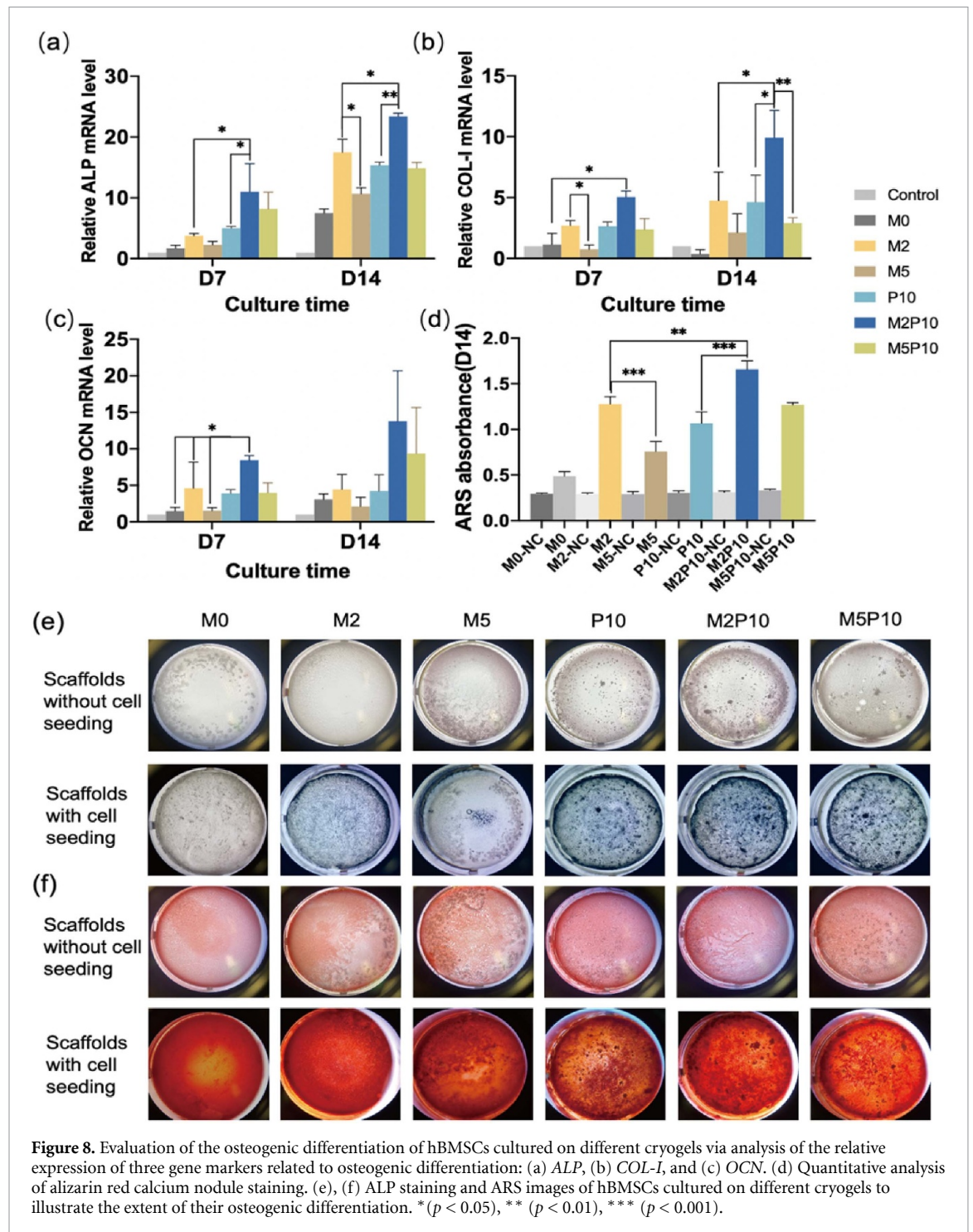
that the M2P10 group displayed the deepest staining. As shown in 8(f), images of ARS at 14 d showed that the M2P10 group had the richest mineral deposits. The ALP and ARS of the cryogel without cell seeding showed only a small amount of staining. Quantitative analysis of ARS showed that there was a significant difference between the cryogels without cell seeding and the cryogels with seeded cells.

### 3.6. Angiogenesis *in vitro* and *in vivo*

Matrigel tube formation assays verified the ability of  $Mg^{2+}$  to promote tube formation *in vitro*. ImageJ software was used to analyze the node numbers and total segment lengths as shown in figures 9(a)–(c). The number of nodes formed by the cells in the M2 group was greater than that in the M5 group, and the total segment length formed by the cells in the P10 group was the smallest among groups. Both of these results showed that the M2P10 group had the most apparent vascular effect.

The expression of the angiogenic gene VEGF was detected by qPCR on the 7th day, as shown in figure 9(d). The expression of VEGF in the M2 group was approximately three-fold that in the M5 group and 1.5-fold that in the P10 group. The expression in the M2P10 group was higher than that in the M2 and P10 groups. And the expression level in the M2P10 group was six times higher than that in the M5P10 group.

Subcutaneous transplantation in nude mice was used to observe the ability of the scaffold materials to promote angiogenesis *in vivo*. According to the conclusions drawn from *in vitro* experiments, the M2P10 cryogel was selected for the experiment using the M0 and M5P10 cryogels as the controls. The overview showed that many blood vessels grew into the cryogel of the M2P10 group, while only a few blood vessels grew into the cryogels of the M0 group and M5P10 group (figure S3). As shown in figures 10(a) and (b), the HE and Masson-stained histological sections that



were collected at 4 w post implantation showed that there was a large amount of blood vessels extending into the pores of the M2P10 cryogel. Figure 10(c) also showed that CD31 were highly expressed in the M2P10 group, which indicated that vascularization occurred in the M2P10 group. In comparison, fewer blood vessels grew in the M5P10 cryogel, and almost no blood vessel grew in the M0 cryogel in the observation field. At a higher magnification, only a small number of blood vessels could be found in the M0 group and M5P10 group. Quantitative analysis of the number of blood vessels had been provided as figure

S4. As for CAM assay, the CAM in M2P10 group also formed the most blood vessels compared with other groups (figure S5).

### 3.7. Critical-sized calvarial defect model

A model of calvarial defect (5 mm in diameter) was established, and the M0 and M2P10 cryogels were implanted to enable exploration of their effects on osteogenesis *in vivo*. The micro-CT reconstruction image as shown in figure 11 shows that at 4 and 8 w, new bone had scarcely formed at the defective area in the control group. At 4 w, the new bone in the M0 and

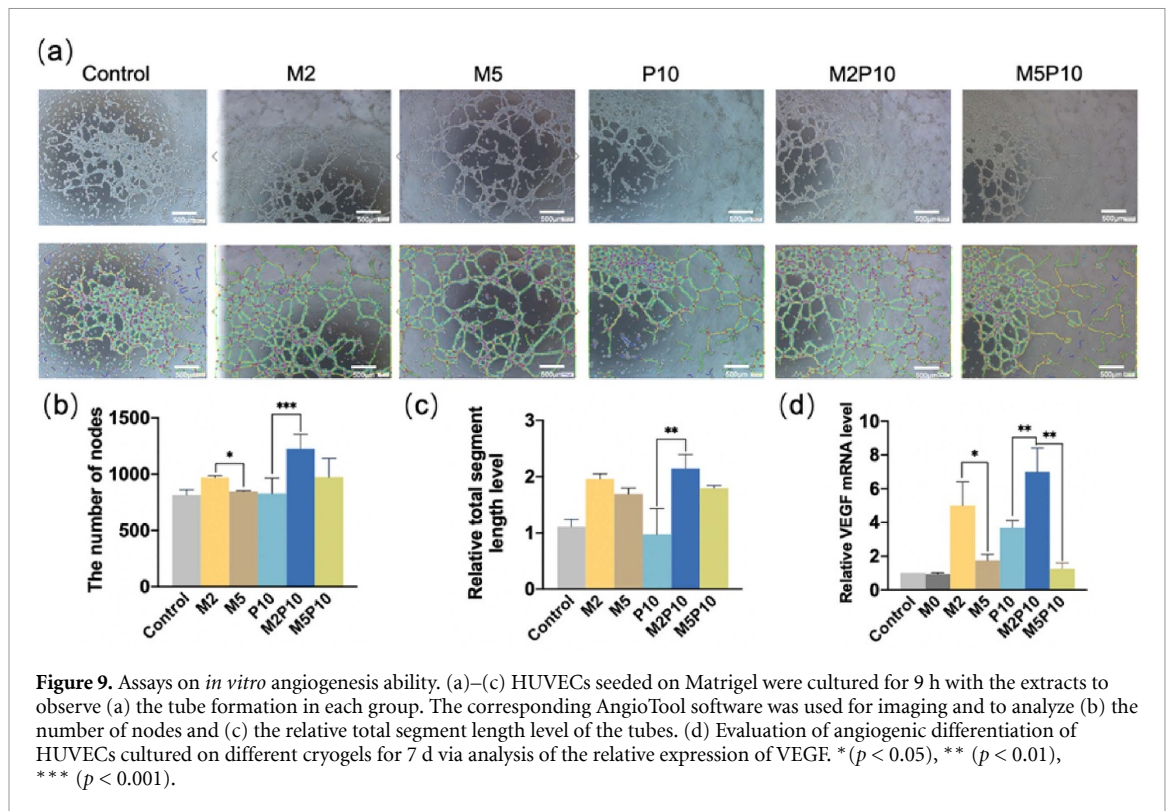


**Figure 9.** Assays on *in vitro* angiogenesis ability. (a)–(c) HUVECs seeded on Matrigel were cultured for 9 h with the extracts to observe (a) the tube formation in each group. The corresponding AngioTool software was used for imaging and to analyze (b) the number of nodes and (c) the relative total segment length level of the tubes. (d) Evaluation of angiogenic differentiation of HUVECs cultured on different cryogels for 7 d via analysis of the relative expression of VEGF. \* ( $p < 0.05$ ), \*\* ( $p < 0.01$ ), \*\*\* ( $p < 0.001$ ).

M2P10 groups began to grow from the periphery to the inside, and the M2P10 group formed more new bone than the M0 group. At 8 w, a small amount of new bone was formed in the M0 group compared with the 4 w group, while the new bone in the M2P10 group had grown to the center of the defect.

Quantitative analysis of the BV/TV ratios and BMD values was carried out based on the micro-CT data. The BV/TV value of the M2P10 group was the highest at 8 weeks, reaching  $40.1 \pm 0.9\%$  at 8 w post implantation, and the BMD value reached  $434.77 \pm 15.89 \text{ mg cm}^{-3}$ . The BV/TV and BMD values of the M0 group were  $23.7 \pm 2.7\%$  and  $238.6 \pm 17.89 \text{ mg cm}^{-3}$ , respectively, and those of the control group were  $13.9 \pm 0.8\%$  and  $136.8 \pm 12.36 \text{ mg cm}^{-3}$ , respectively.

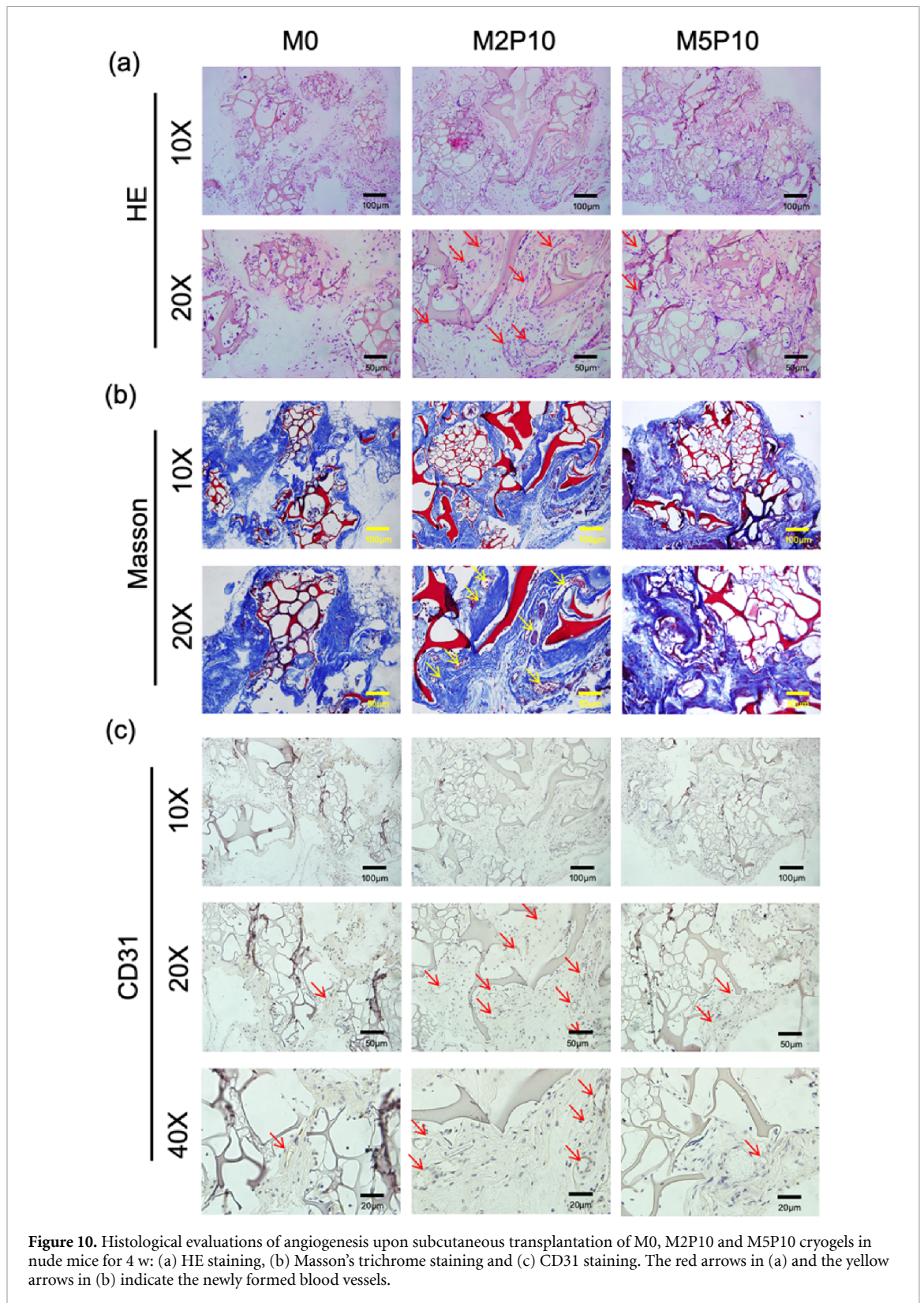
As shown in figure S6, the supplementary provides three parallel control groups of the HE-stained histological sections at 8 w, and finally we integrated all the characteristics to select a group of representative results. As shown in the figure 12, HE and Masson staining showed that the most significant osteogenesis occurred in the M2P10 group. In the tissue sections of the control group at 4 and 8 w, it was observed that only a small amount of new bone was formed at the defect boundary, and the defect area was surrounded by fibrous connective tissue. At 4 w, new bone was formed in the M2P10 group, and there was residual cryogel around the new bone, with many blood vessels around it. The cryogel could be seen in the M0 group, but the new bone formation was less than that in the M2P10 group. At 8 w, more new bone was formed in the M2P10 group

than in the M0 group, and the bone tended to grow to the center of the defect, while only scattered new bone was formed in the M0 group. Immunohistochemical staining in figure 13 also showed that CD31 and OCN were highly expressed in the M2P10 group, which indicated that vascularization and osteogenesis occurred in the M2P10 group.

#### 4. Discussion

Angiogenesis plays a vital role in bone tissue repair. Ions co-delivery systems are expected to achieve successful bone regeneration by firstly promoting angiogenesis [51]. In this study, we applied a GelMA cryogel and PLGA microspheres as the matrixes to co-delivery of  $\text{Mg}^{2+}$  and  $\text{La}^{3+}$  in order to stimulate angiogenesis and osteogenesis in bone defects.

The GelMA cryogel fabricated with large pore sizes can enable oxygen and nutrients to be provided in the core of the scaffold, thus contributing to sufficient angiogenesis [52]. Moreover,  $\text{Mg}^{2+}$  loaded in the cryogel can be released in the early stage because the cryogel is hydrophilic. Since  $\text{MgO}$  dissolves faster than  $\text{MgCO}_3$ , it can achieve a moderate release effect to promote vascularized bone regeneration in the early stage [24].  $\text{La}_2(\text{CO}_3)_3$  was wrapped in PLGA microspheres, which are often used as carriers to control the release of drugs or metal ions [53]. Loading the microspheres into the GelMA cryogel can further delay the release of  $\text{La}^{3+}$  and enable dual delivery of the two metal ions in chronological order. During the process of gradual degradation of the cryogel, the PLGA microspheres degrade



relatively slowly, which can also play a supporting role. From 0 to 12 w, the intensity of  $\text{La}^{3+}$  signal in mapping images continuously decreased, indicating the sustained release of  $\text{La}^{3+}$  alongside scaffold degradation. Since the complete degradation of PLGA might take about 6 months [54], it was suggested that the long-term release of  $\text{La}^{3+}$  would favor new bone formation at later stage. Studies have shown

that the accumulation of a small amount of lanthanide elements in bones can and inhibit bone degradation [30], therefore, even a burst release of  $\text{La}^{3+}$  occurred after the complete degradation of PLGA, it would not cause significant adverse effect to the body since the total amount of the introduced  $\text{La}_2(\text{CO}_3)_3$  was not high (5 mg cryogel contains 0.05 mg  $\text{La}_2(\text{CO}_3)_3$ ).

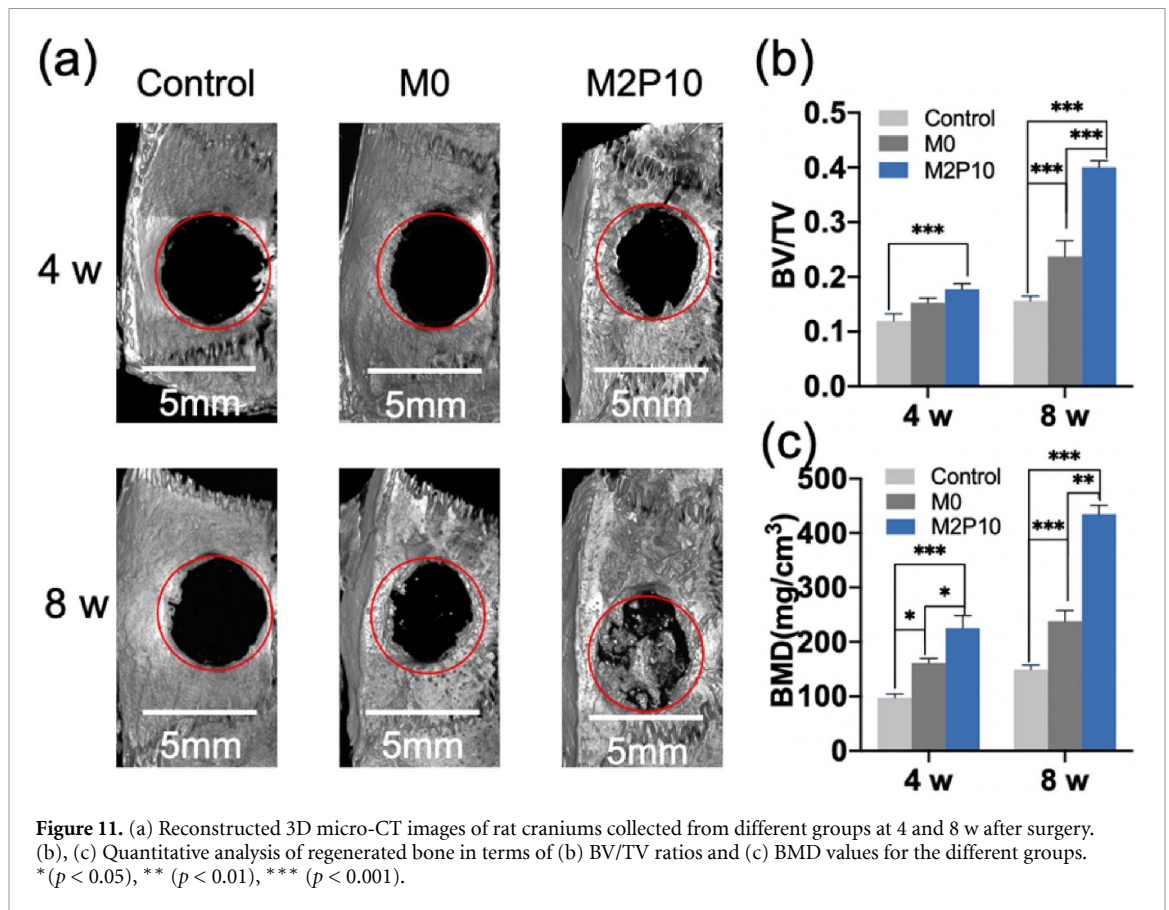


**Figure 11.** (a) Reconstructed 3D micro-CT images of rat craniums collected from different groups at 4 and 8 w after surgery. (b), (c) Quantitative analysis of regenerated bone in terms of (b) BV/TV ratios and (c) BMD values for the different groups. \* ( $p < 0.05$ ), \*\* ( $p < 0.01$ ), \*\*\* ( $p < 0.001$ ).

The combined results of the ion release assay and the Alamar blue assay indicated that the cell proliferation in the M2 group was faster than that in the M5 group. Studies have shown that  $Mg^{2+}$  concentrations within 10 mM can promote cell proliferation and migration [55]. In the M5 group, cell proliferation was inhibited at the early stage, and the cell proliferation rate was increased on the 7th day. This may be because the medium pH value of the M5 group was relative high during the early burst release [56]. With the continuous release of ions, the pH value gradually decreased due to dilution by new PBS, and the cell proliferation was accelerated at later stage. The number of migrating cells in the M2 group was significantly higher than that in the M5 group, indicating that the  $Mg^{2+}$  concentration of the M2 extract showed stronger ability in promoting cell migration than that of the M5 extract, and the M2 cryogel might be conducive to cell migration in the early stage of injury [57]. At a proper concentration,  $Mg^{2+}$  can enhance cell motility, which is an essential part of angiogenesis, inflammation, normal development and tissue repair [58].

With regard to angiogenesis, the results of the Matrigel tube formation assay indicated that more tubes formed in the M2 group than in the M5 group and P10 group. Furthermore, the angiogenic gene expression levels led to the same conclusion.  $Mg^{2+}$  can promote angiogenesis by simulating hypoxic

conditions and contributing to the transcription of VEGF [18, 59]. Altogether, the above three *in vitro* experiments proved that  $Mg^{2+}$  can promote cell migration and promote angiogenesis in the early stage. To further prove the vascularization effects of the scaffolds, we performed subcutaneous transplantation and observed the effects on vascularization. HE and Masson staining of tissue slices indicated that the M0 group did not exhibit much vascularization. In contrast, the M2P10 group had greater promotion of blood vessels, and more blood vessels grew into the cryogels in the M2P10 group than in the M0 group. Activation of endothelial cells during angiogenesis requires cell diffusion and migration. Studies have shown that  $Mg^{2+}$  can be recognized by endothelial cells [60].  $Mg^{2+}$  can stimulate proliferation and make microvascular cells sensitive to migration signals, thereby inducing angiogenesis [61]. Lai *et al* found that PLGA/ $\beta$ -tricalcium phosphate/Mg scaffolds can promote the inward growth of new blood vessels at 4 w and that large numbers of newly formed blood vessels were present at 8 w in a segmental ulnar bone defect model [62].

The cell proliferation of the P10 group was significantly higher than that of the control and P20 groups. In the P10 group, the release of  $La^{3+}$  increased from the 4th day and reached a peak at 7–14 d at approximately  $100 \mu g L^{-1}$ . Previous studies have shown that a  $La^{3+}$  concentration

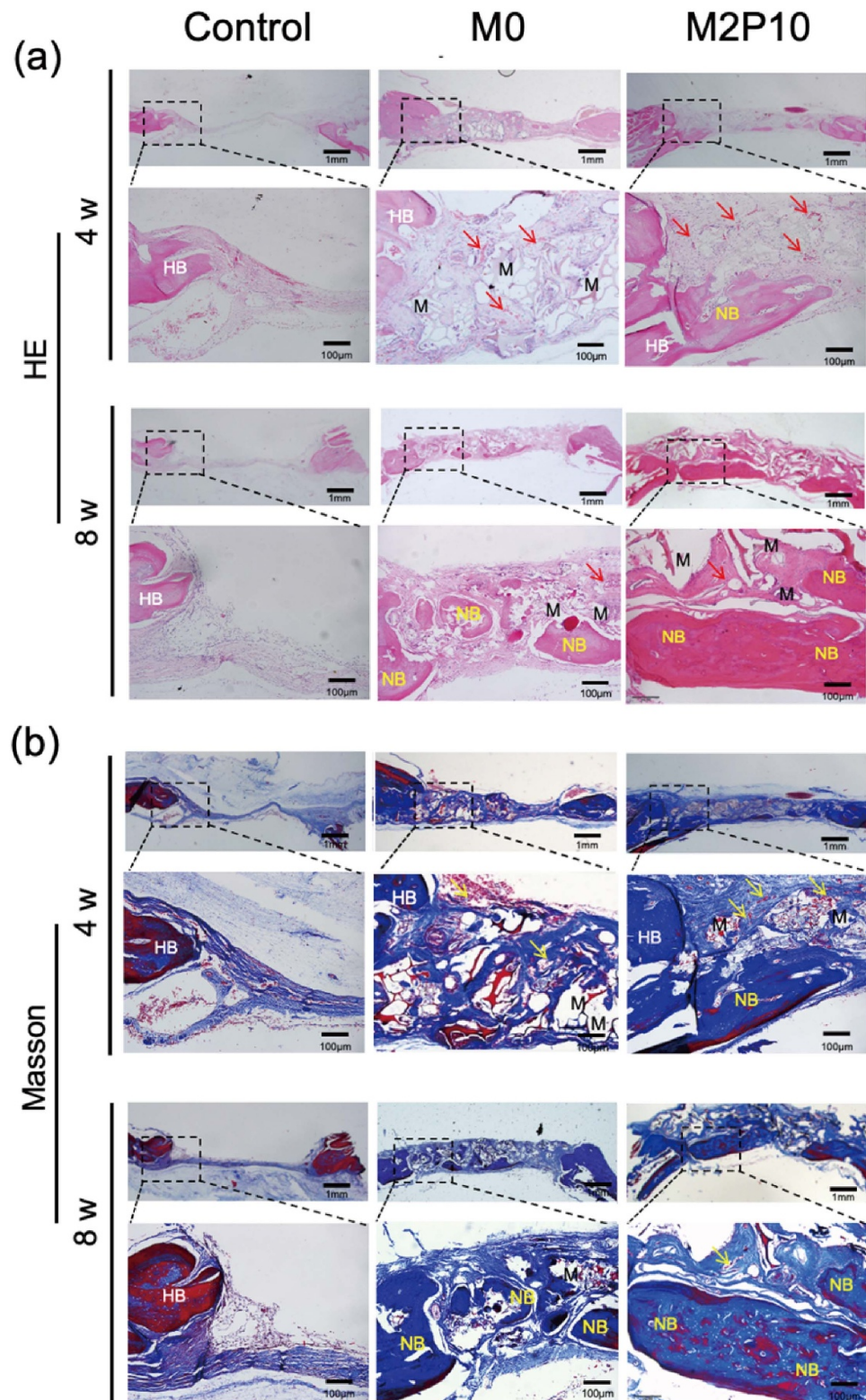


**Figure 12.** Histological evaluations of bone regeneration at 4 and 8 w for the control, M0 and M2P10 groups. (a) HE staining, (b) Masson's trichrome staining were performed. Arrows: the newly formed blood vessels. HB, host bone; NB, newly formed bone; M, residual scaffolds.

of  $10^{-9}$ – $10^{-7}$  M can promote cell proliferation [63]. When the  $\text{La}^{3+}$  concentration is elevated, it can inhibit cell proliferation and differentiation [31]. Therefore, the P10 group was selected as the experimental group for subsequent experiments. In P10 group, osteogenic differentiation of cells was

promoted *in vitro*, and the expression of bone-related genes in the P10 group was significantly higher than that in the M0 group. Low concentrations of  $\text{La}^{3+}$  can upregulate *ALP*, *OCN* and *COL-1* gene expression in hBMSCs [64]. Moreover, the results of ALP and ARS also confirmed this effect.  $\text{La}^{3+}$  in composite scaffolds

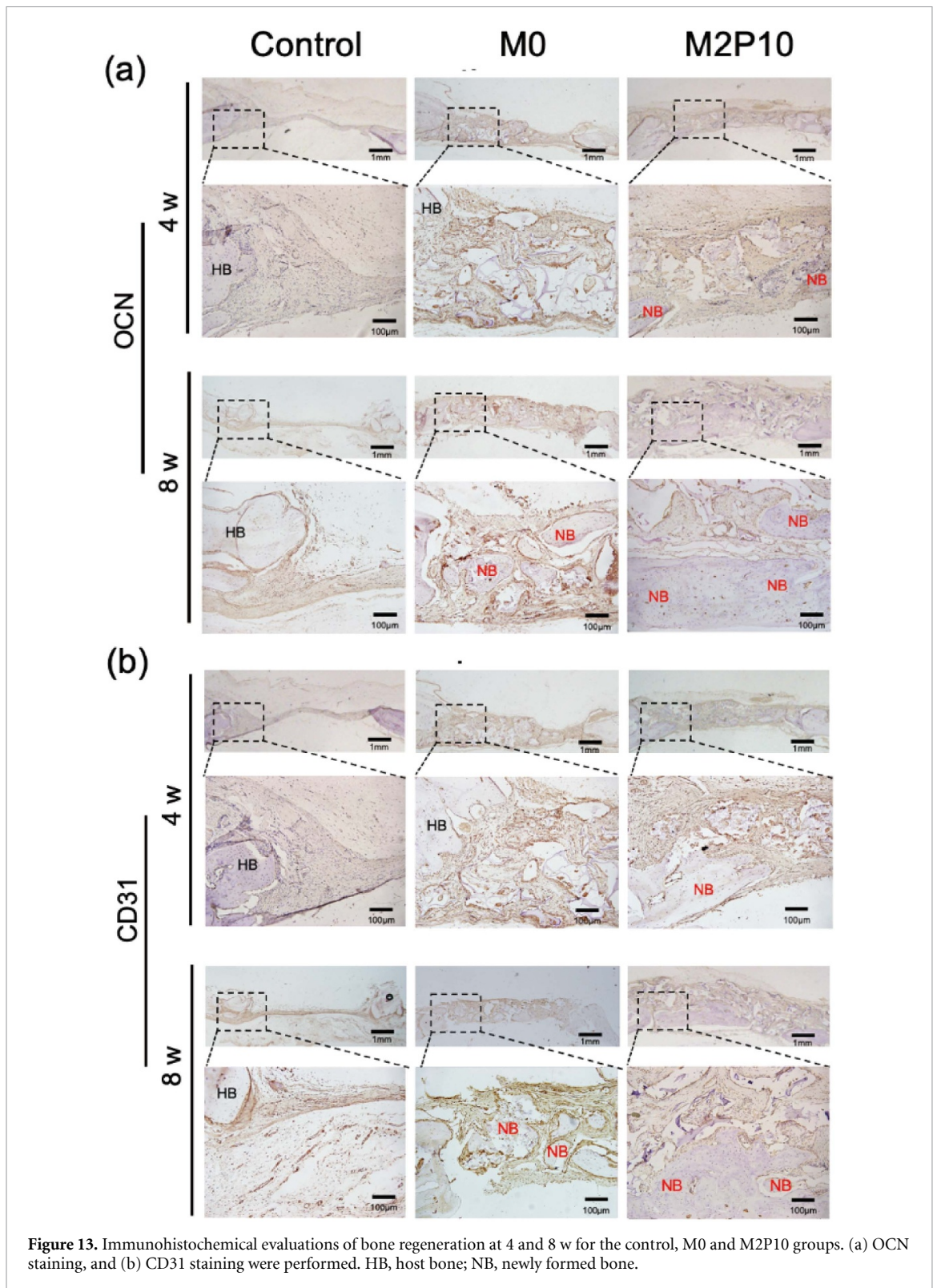


**Figure 13.** Immunohistochemical evaluations of bone regeneration at 4 and 8 w for the control, M0 and M2P10 groups. (a) OCN staining, and (b) CD31 staining were performed. HB, host bone; NB, newly formed bone.

may play a significant role in promoting osteogenic differentiation [65]. The effect of  $\text{La}^{3+}$  on osteoblast activity is concentration-dependent and time-dependent. Low concentrations of  $\text{La}^{3+}$  stimulate the expression of osteoblast-specific genes; increase ALP activity, OCN secretion and matrix mineralization; and promote the differentiation of osteoblasts *in vitro* [66].

The Alamar blue assay, live/dead staining and phalloidin-Hoechst/DAPI staining all showed that the M2P10 group had the best cell proliferation, and the cryogel in this group had good biocompatibility. In the *in vitro* osteogenic differentiation experiment, we observed that the M2P10 group had the best effect with the highest expressions of osteogenic genes; the expression in this group was approximately



twice that in the M2 group and P10 group. Moreover, the expression of VEGF in the M2P10 group was significantly higher than those in the M2 group and P10 group. The combined results of osteogenic and angiogenic gene expression indicate that  $Mg^{2+}$  and  $La^{3+}$  may have synergistic effects on vascularization and bone formation. Altogether, the *in vitro* experiments proved that the co-delivery of  $Mg^{2+}$  and  $La^{3+}$  had better angiogenic and osteogenic effects than the delivery of either ion individually. The *in vitro* differentiation data was analyzed by the method presented in the figure S7. When  $P_{observed} > P_{expected}$ , a synergistic effect for the two ions is achieved rather than an additive effect. According to the heat map analysis (figure S8), compared with the M2 and P10 groups, M2P10 has a synergistic effect in promoting cell proliferation, promoting angiogenesis and promoting osteogenesis.

As stated above, compared to single-ion systems, we have confirmed that the M2P10 group has the best osteogenic capability compared to the M2 and P10 group. Therefore, according to the welfare requirements of experimental animals to reduce the number of animals, we selected M2P10 group with the best effect on promoting angiogenesis and osteogenesis *in vitro* as the experimental group *in vivo*. As for *in situ* osteogenesis experiment, at 8 w, the BV/TV value of the M2P10 group was  $16.4 \pm 1.9\%$  higher than that of the M0 group, and the BMD value of the M2P10 group was  $196.1 \pm 2 \text{ mg cm}^{-3}$  higher than that of the M0 group, indicating that loading of  $Mg^{2+}$  and  $La^{3+}$  can enhance osteogenesis. In the tissue sections, there were more blood vessels around the new bone of the skull defect in the M2P10 group than in other groups. In the M0 group, small amounts of blood vessel formation and new bone formation could also be observed, indicating that the M0 cryogel has limited capacity in promoting bone regeneration. In a previous study with good experimental results, when magnesium was incorporated into calcium silicate, the BV/TV was 35% at 12 w for a 5 mm bone defect and was approximately 10% higher than that of the calcium silicate group [67]. Li *et al* found that when MgO was loaded into polymethylmethacrylate (PMMA), the BV/TV achieved in the MgO/PMMA group ( $12.70 \pm 1.85\%$ ) was significantly greater than that in the PMMA group ( $9.61 \pm 2.66\%$ ) at 12 w for a 5 mm bone defect [68]. In another study, Hu *et al* found that when  $La_2(CO_3)_3$  was incorporated into chitosan, the BV/TV value of the La-loaded group was  $12.02 \pm 0.47\%$  higher than that of the simple chitosan group at 12 w for a 5 mm bone defect [35]. According to our results, apart from the influences of the materials on osteogenesis,  $Mg^{2+}$  and  $La^{3+}$  can promote vascularization better than either ion acting alone. In the long-term process of bone reconstruction, the persisting supply of low dose of  $La^{3+}$  may achieve a durable effect on promoting osteogenesis. On the other hand, only about 0.05 mg of  $La_2(CO_3)_3$  was

added into each hole of the rat skull defect. Even as the PLGA microspheres totally degraded at 6–12 months post-implantation to release the residual  $La^{3+}$  in a sudden at the later stage [54], it would not cause significant adverse effect as studies have shown that the accumulation of a small amount of lanthanide elements in bones can stimulate bone formation and inhibit bone degradation, without causing toxicity to the body [30]. Combined with the conclusions drawn from *in vitro* experiments, the co-delivery of  $Mg^{2+}$  and  $La^{3+}$  has a synergistic effect on promoting vascularization and bone regeneration. Given these findings and those of the *in vivo* experiments, we can conclude that  $Mg^{2+}$  and  $La^{3+}$  have a synergistic effect on the regeneration of vascularized bone tissue benefiting from their co-delivery pattern via using the GelMA cryogel-PLGA microsphere system.

## 5. Conclusion

In this research, we successfully prepared an ion co-delivery system. MgO and  $MgCO_3$  were directly mixed into GelMA cryogel at a ratio of 1:1, which allowed  $Mg^{2+}$  to be released firstly.  $La_2(CO_3)_3$  was wrapped in PLGA microspheres and then mixed into the GelMA cryogel to achieve a slow-release of  $La^{3+}$ . According to the experimental results, we found that  $Mg^{2+}$  and  $La^{3+}$  can promote bone regeneration through the controlled release. The co-delivery of  $Mg^{2+}$  and  $La^{3+}$  have a synergistic effect in promoting vascularized bone formation, suggesting the GelMA cryogel-PLGA microsphere system to be a promising strategy for the purpose. In future, the mechanism/signaling pathway by which  $Mg^{2+}$  and  $La^{3+}$  promote vascularization and bone formation will be explored with more details via cellular and molecular assays.

## Data availability statement

All data that support the findings of this study are included within the article (and any supplementary files).

## Acknowledgments

This research was supported by Beijing Natural Science Foundation(7212135), China.

## Conflict of interest

The authors declare no competing financial interest.

## ORCID iDs

Yuming Zhao  <https://orcid.org/0000-0002-2395-6254>

Qing Cai  <https://orcid.org/0000-0001-6618-0321>

## References

- [1] Saran U, Gemini Piperni S and Chatterjee S 2014 Role of angiogenesis in bone repair *Arch. Biochem. Biophys.* **561** 109–17
- [2] Stegen S and Carmeliet G 2018 The skeletal vascular system—breathing life into bone tissue *Bone* **115** 50–58
- [3] Rouwkema J, Rivron N C and Van Blitterswijk C A 2008 Vascularization in tissue engineering *Trends Biotechnol.* **26** 434–41
- [4] Bayer E A, Gottardi R, Fedorchak M V and Little S R 2015 The scope and sequence of growth factor delivery for vascularized bone tissue regeneration *J. Control. Release* **219** 129–40
- [5] Zhang B, Li H, He L, Han Z, Zhou T, Zhi W, Lu X, Lu X and Weng J 2018 Surface-decorated hydroxyapatite scaffold with on-demand delivery of dexamethasone and stromal cell derived factor-1 for enhanced osteogenesis *Mater. Sci. Eng. C* **89** 355–70
- [6] Dashtimoghadam E, Fahimipour F, Tongas N and Tayebi L 2020 Microfluidic fabrication of microcarriers with sequential delivery of VEGF and BMP-2 for bone regeneration *Sci. Rep.* **10** 11764
- [7] Farokhi M, Mottaghitalab F, Shokrgozar M A, Ou K L, Mao C and Hosseinkhani H 2016 Importance of dual delivery systems for bone tissue engineering *J. Control. Release* **225** 152–69
- [8] Park J Y, Shim J H, Choi S A, Jang J, Kim M, Lee S H and Cho D W 2015 3D printing technology to control BMP-2 and VEGF delivery spatially and temporally to promote large-volume bone regeneration *J. Mater. Chem. B* **3** 5415–25
- [9] Lee S S, Kim J H, Jeong J, Kim S H L, Koh R H, Kim I, Bae S, Lee H and Hwang N S 2020 Sequential growth factor releasing double cryogel system for enhanced bone regeneration *Biomaterials* **257** 120223
- [10] Kim Y H and Tabata Y 2015 Dual-controlled release system of drugs for bone regeneration *Adv. Drug Deliv. Rev.* **94** 28–40
- [11] Weng L, Boda S K, Teusink M J, Shuler F D, Li X and Xie J 2017 Binary doping of strontium and copper enhancing osteogenesis and angiogenesis of bioactive glass nanofibers while suppressing osteoclast activity *ACS Appl. Mater. Interfaces* **9** 24484–96
- [12] Glenske K et al 2018 Applications of metals for bone regeneration *Int. J. Mol. Sci.* **19** 826
- [13] Mourino V, Cattalini J P and Boccaccini A R 2012 Metallic ions as therapeutic agents in tissue engineering scaffolds: an overview of their biological applications and strategies for new developments *J. R. Soc. Interface* **9** 401–19
- [14] Zhou J, Wang X and Zhao L 2019 Antibacterial, angiogenic, and osteogenic activities of Ca, P, Co, F, and Sr compound doped titania coatings with different Sr content *Sci. Rep.* **9** 14203
- [15] Zhao Q, Yi L, Hu A, Jiang L, Hong L and Dong J 2019 Antibacterial and osteogenic activity of a multifunctional microporous coating codoped with Mg, Cu and F on titanium *J. Mater. Chem. B* **7** 2284–99
- [16] Nabyouni M, Bruckner T, Zhou H, Gbureck U and Bhaduri S B 2018 Magnesium-based bioceramics in orthopedic applications *Acta Biomater.* **66** 23–43
- [17] Bose S, Tarafder S and Bandyopadhyay A 2017 Effect of chemistry on osteogenesis and angiogenesis towards bone tissue engineering using 3D printed scaffolds *Ann. Biomed. Eng.* **45** 261–72
- [18] Yoshizawa S, Brown A, Barchowsky A and Sfeir C 2014 Magnesium ion stimulation of bone marrow stromal cells enhances osteogenic activity, simulating the effect of magnesium alloy degradation *Acta Biomater.* **10** 2834–42
- [19] Maier J A, Bernardini D, Rayssiguier Y and Mazur A 2004 High concentrations of magnesium modulate vascular endothelial cell behaviour *in vitro Biochim. Biophys. Acta* **1689** 6–12
- [20] Banai S, Haggroth L, Epstein S E and Casscells W 1990 Influence of extracellular magnesium on capillary endothelial cell proliferation and migration *Circ. Res.* **67** 645–50
- [21] Choi S, Kim K J, Cheon S, Kim E M, Kim Y A, Park C and Kim K K 2020 Biochemical activity of magnesium ions on human osteoblast migration *Biochem. Biophys. Res. Commun.* **531** 588–94
- [22] Bernardini D, Nasulewicz A, Mazur A and Maier J A 2005 Magnesium and microvascular endothelial cells: a role in inflammation and angiogenesis *Front. Biosci.* **10** 1177–82
- [23] Diaz-Tocados J M et al 2017 Magnesium chloride promotes osteogenesis through notch signaling activation and expansion of mesenchymal stem cells *Sci. Rep.* **7** 7839
- [24] Yuan Z, Wei P, Huang Y, Zhang W, Chen F, Zhang X, Mao J, Chen D, Cai Q and Yang X 2019 Injectable PLGA microspheres with tunable magnesium ion release for promoting bone regeneration *Acta Biomater.* **85** 294–309
- [25] Liu C, Fu X, Pan H, Wan P, Wang L, Tan L, Wang K, Zhao Y, Yang K and Chu P K 2016 Biodegradable Mg-Cu alloys with enhanced osteogenesis, angiogenesis, and long-lasting antibacterial effects *Sci. Rep.* **6** 27374
- [26] Lin Z et al 2018 Precisely controlled delivery of magnesium ions thru sponge-like monodisperse PLGA/nano-MgO-alginate core-shell microsphere device to enable *in-situ* bone regeneration *Biomaterials* **174** 1–16
- [27] Yu K et al 2018 *In vitro* and *in vivo* evaluation of novel biodegradable Mg-Ag-Y alloys for use as resorbable bone fixation implant *J. Biomed. Mater. Res. A* **106** 2059–69
- [28] Jiang C et al 2016 Lanthanum chloride attenuates osteoclast formation and function via the downregulation of rankl-induced Nf-kappab and Nfatc1 activities *J. Cell. Physiol.* **231** 142–51
- [29] Liu D, Ge K, Sun J, Chen S, Jia G and Zhang J 2015 Lanthanum breaks the balance between osteogenesis and adipogenesis of mesenchymal stem cells through phosphorylation of Smad1/5/8 *RSC Adv.* **5** 42233–41
- [30] Wieszczycka K, Staszak K, Woźniak-Budych M J and Jurga S 2019 Lanthanides and tissue engineering strategies for bone regeneration *Coord. Chem. Rev.* **388** 248–67
- [31] Bai J, Wang X H, Zhang C J, Huang J and Muller W E G 2018 Lanthanum-containing bioparticles are associated with the influence of lanthanum on high phosphate mediated bone marrow stromal cells viability *Biomaterials* **31** 771–84
- [32] Cheng S et al 2013 Effects of extracellular calcium on viability and osteogenic differentiation of bone marrow stromal cells *in vitro Hum. Cell* **26** 114–20
- [33] Gautam C R, Kumar S, Mishra V K and Biradar S 2017 Synthesis, structural and 3D architecture of lanthanum oxide added hydroxyapatite composites for bone implant applications: enhanced microstructural and mechanical properties *Ceram. Int.* **43** 14114–21
- [34] Wang X, Yuan L, Huang J, Zhang T L and Wang K 2008 Lanthanum enhances *in vitro* osteoblast differentiation via pertussis toxin-sensitive gi protein and ERK signaling pathway *J. Cell. Biochem.* **105** 1307–15
- [35] Hu H, Zhao P, Liu J, Ke Q, Zhang C, Guo Y and Ding H 2018 Lanthanum phosphate/chitosan scaffolds enhance cytocompatibility and osteogenic efficiency via the Wnt/beta-catenin pathway *J. Nanobiotechnol.* **16** 98
- [36] Peng X Y, Hu M, Liao F, Yang F, Ke Q F, Guo Y P and Zhu Z H 2019 La-doped mesoporous calcium silicate/chitosan scaffolds for bone tissue engineering *Biomater. Sci.* **7** 1565–73
- [37] Rather H A, Jhala D and Vasita R 2019 Dual functional approaches for osteogenesis coupled angiogenesis in bone tissue engineering *Mater. Sci. Eng. C* **103** 109761
- [38] Luo Z et al 2018 Time-responsive osteogenic niche of stem cells: a sequentially triggered, dual-peptide loaded, alginate hybrid system for promoting cell activity and osteo-differentiation *Biomaterials* **163** 25–42
- [39] Wang K, Cheng W, Ding Z, Xu G, Zheng X, Li M, Lu G and Lu Q 2020 Injectable silk/hydroxyapatite nanocomposite

- hydrogels with vascularization capacity for bone regeneration *J. Mater. Sci. Technol.* **63** 172–81
- [40] Rambhia K J and Ma P X 2015 Controlled drug release for tissue engineering *J. Control. Release* **219** 119–28
- [41] Sivashanmugam A, Charoenlarp P, Deepthi S, Rajendran A, Nair S V, Iseki S and Jayakumar R 2017 Injectable shear-thinning CaSO<sub>4</sub>/FGF-18-Incorporated chitin-PLGA hydrogel enhances bone regeneration in mice cranial bone defect model *ACS Appl. Mater. Interfaces* **9** 42639–52
- [42] Gu B, Sun X, Papadimitrakopoulos F and Burgess D J 2016 Seeing is believing, PLGA microsphere degradation revealed in PLGA microsphere/PVA hydrogel composites *J. Control. Release* **228** 170–8
- [43] Yue K, Trujillo-de Santiago G, Alvarez M M, Tamayol A, Annabi N and Khademhosseini A 2015 Synthesis, properties, and biomedical applications of gelatin methacryloyl (GelMA) hydrogels *Biomaterials* **73** 254–71
- [44] Khayat A, Monteiro N, Smith E E, Pagni S, Zhang W, Khademhosseini A and Yelick P C 2017 GelMA-encapsulated hDPSCs and HUVECs for dental pulp regeneration *J. Dent. Res.* **96** 192–9
- [45] Gu L, Zhang J, Li L, Du Z, Cai Q and Yang X 2019 Hydroxyapatite nanowire composited gelatin cryogel with improved mechanical properties and cell migration for bone regeneration *Biomed. Mater.* **14** 045001
- [46] Hixon K R, Lu T and Sell S A 2017 A comprehensive review of cryogels and their roles in tissue engineering applications *Acta Biomater.* **62** 29–41
- [47] Danhier F, Ansorena E, Silva J M, Coco R, Le Breton A and Preat V 2012 PLGA-based nanoparticles: an overview of biomedical applications *J. Control. Release* **161** 505–22
- [48] Ding D and Zhu Q 2018 Recent advances of PLGA micro/nanoparticles for the delivery of biomacromolecular therapeutics *Mater. Sci. Eng. C* **92** 1041–60
- [49] Zhang L, Wang Z, Xiao Y, Liu P, Wang S, Zhao Y, Shen M and Shi X 2018 Electrospun PEGylated PLGA nanofibers for drug encapsulation and release *Mater. Sci. Eng. C* **91** 255–62
- [50] Mir M, Ahmed N and Rehman A U 2017 Recent applications of PLGA based nanostructures in drug delivery *Colloids Surf. B* **159** 217–31
- [51] Mao L, Xia L, Chang J, Liu J, Jiang L, Wu C and Fang B 2017 The synergistic effects of Sr and Si bioactive ions on osteogenesis, osteoclastogenesis and angiogenesis for osteoporotic bone regeneration *Acta Biomater.* **61** 217–32
- [52] Seyednejad H, Gawlitta D, Kuiper R V, De Bruin A, Van Nostrum C F, Vermonden T, Dhert W J and Hennink W E 2012 *In vivo* biocompatibility and biodegradation of 3D-printed porous scaffolds based on a hydroxyl-functionalized poly(epsilon-caprolactone) *Biomaterials* **33** 4309–18
- [53] Martins C, Sousa F, Araujo F and Sarmiento B 2018 Functionalizing PLGA and PLGA derivatives for drug delivery and tissue regeneration applications *Adv. Healthc. Mater.* **7** 1701035
- [54] Kapoor D N, Bhatia A, Kaur R, Sharma R, Kaur G and Dhawan S 2015 PLGA: a unique polymer for drug delivery *Ther. Deliv.* **6** 41–58
- [55] Gu Y, Zhang J, Zhang X, Liang G, Xu T and Niu W 2019 Three-dimensional printed Mg-doped beta-TCP bone tissue engineering scaffolds: effects of magnesium ion concentration on osteogenesis and angiogenesis *in vitro Tissue Eng. Regen. Med.* **16** 415–29
- [56] Marx D, Yazdi A R, Papini M and Towler M 2020 *In vitro* osteogenic performance of two novel strontium and zinc-containing glass polyalkenoate cements *J. Biomed. Mater. Res. A* **109** 1366–78
- [57] Pan S, An L, Meng X, Li L, Ren F and Guan Y 2017 MgCl<sub>2</sub> and ZnCl<sub>2</sub> promote human umbilical vein endothelial cell migration and invasion and stimulate epithelial-mesenchymal transition via the Wnt/beta-catenin pathway *Exp. Ther. Med.* **14** 4663–70
- [58] Kim K J, Choi S, Sang Cho Y, Yang S J, Cho Y S and Kim K K 2017 Magnesium ions enhance infiltration of osteoblasts in scaffolds via increasing cell motility *J. Mater. Sci. Mater. Med.* **28** 96
- [59] Xu L, Willumeit-Romer R and Luthringer-Feyerabend B 2020 Hypoxia influences the effects of magnesium degradation products on the interactions between endothelial and mesenchymal stem cells *Acta Biomater.* **101** 624–36
- [60] Lapidus K A, Woodhouse E C, Kohn E C and Masiero L 2001 Mg(++)-induced endothelial cell migration: substratum selectivity and receptor-involvement *Angiogenesis* **4** 21–28
- [61] Coelho C C, Padrao T, Costa L, Pinto M T, Costa P C, Domingues V F, Quadros P A, Monteiro F J and Sousa S R 2020 The antibacterial and angiogenic effect of magnesium oxide in a hydroxyapatite bone substitute *Sci. Rep.* **10** 19098
- [62] Lai Y et al 2019 Osteogenic magnesium incorporated into PLGA/TCP porous scaffold by 3D printing for repairing challenging bone defect *Biomaterials* **197** 207–19
- [63] Liu D, Zhang J, Wang G, Liu X, Wang S and Yang M 2012 The dual-effects of LaCl<sub>3</sub> on the proliferation, osteogenic differentiation, and mineralization of MC3T3-E1 cells *Biol. Trace Elem. Res.* **150** 433–40
- [64] Zhang X et al 2020 Synergistic effects of lanthanum and strontium to enhance the osteogenic activity of TiO<sub>2</sub> nanotube biological interface *Ceram. Int.* **31** 771–84
- [65] Bochicchio B, Barbaro K, De Bonis A, Rau J V and Pepe A 2020 Electrospun poly(D, L-lactide)/gelatin/glass-ceramics tricomponent nanofibrous scaffold for bone tissue engineering *J. Biomed. Mater. Res. A* **108** 1064–76
- [66] Zhang S, Liu Q, Li L, Bai Y and Yang B 2018 The controllable lanthanum ion release from Ca-P coating fabricated by laser cladding and its effect on osteoclast precursors *Mater. Sci. Eng. C* **93** 1027–35
- [67] Du Z, Leng H, Guo L, Huang Y, Zheng T, Zhao Z, Liu X, Zhang X, Cai Q and Yang X 2020 Calcium silicate scaffolds promoting bone regeneration via the doping of Mg<sup>2+</sup> or Mn<sup>2+</sup> ion *Composites B* **190** 107937
- [68] Li C, Sun J, Shi K, Long J, Li L, Lai Y and Qin L 2020 Preparation and evaluation of osteogenic nano-MgO/PMMA bone cement for bone healing in a rat critical size calvarial defect *J. Mater. Chem. B* **8** 4575–86